Theses and Dissertations

5-2017

Effect of Column Axial Load on Skewed SMF RBS Connection Demands

Clovis Desrochers
University of Arkansas, Fayetteville

Effect of Column Axial Load on Skewed SMF
RBS Connection Demands

A thesis submitted in partial fulfillment
of the requirements for the degree of
Master of Science in Civil Engineering

by

Clovis Desrochers
University of Arkansas
Bachelor of Science in Civil Engineering, 2015

May 2017
University of Arkansas

This thesis is approved for recommendation to the Graduate Council.

_____
Dr. Gary Prinz
Thesis Director

_____   _____
Dr. Eric Fernstrom   Dr. Micah Hale
Committee Member   Committee Member

Abstract

Steel buildings in high seismic areas often require special structural systems to transfer large lateral forces induced by earthquake accelerations. The selection of an appropriate seismic steel system (braced frame, moment frame, shear wall, etc.) is often influenced by architectural considerations. Moment frame configurations offer the most architectural flexibility, but are limited by code prequalification requirements that limit the use of non-orthogonal (skewed) beam-column connection geometries. A recent study has investigated laterally skewed moment frame connections, indicating that skew increases the potential for column twist and column flange yielding; however, it is unclear how realistic column axial loads will affect the skewed connection performance.

This study investigates the effects of column axial loads on skewed special moment frame connections containing reduced beam sections (RBSs). Detailed finite element analyses are used for all investigations, and several beam-column connection configurations are considered, representing: 3 beam-column geometries (shallow, medium and deep columns); 4 levels of skew at the beam-to-column connection; and 4 levels of applied column axial load. Results indicate that combined beam skew, axial load, and applied connection rotations lead to local buckling issues within deep column moment frame configurations; however, increasing beam-skew and axial load has little effect on connection moment capacity prior to column local buckling initiation. Beam-skew angle is the dominate contributor to resulting column twist and increasing column axial load (up to 50% ΦP_n) has a negligible effect on resulting column twist. Applied column axial loads have little effect on resulting column flange yielding within the skewed beam-to-column connections.

Table of Contents

List of Tables

List of Figures

1. Introduction:

Steel buildings in high seismic areas often require special structural systems to transfer large lateral forces induced by earthquake accelerations. These structural systems include specially detailed moment frames (called special moment frames (SMFs)) having connection regions capable of providing adequate lateral stiffness and ductility. One common SMF connection detail involves a reduced beam section (RBS) wherein a portion of the beam flange is removed to prevent large forces from developing at the beam-column connection welds (see Figure 1) [Hamburger et al. 2009]. SMFs with RBS flange cuts were developed following the 1994 Northridge Earthquake [Engelhardt and Sabol (1997), Lee et al. (2005), Tsai et al. (1995), Ricles et al. (2003), Zhang and Ricles (2006)], which produced unanticipated moment frame connection fractures as shown in Figure 2 [FEMA (2000)].

The selection of an appropriate seismic steel system (braced frame, moment frame, shear wall, etc.) is often influenced by architectural considerations. For example, braced frames provide adequate lateral stiffness and high system ductility to resist seismic demands, but have diagonal frame elements which can interfere with the building's architectural objectives (unobstructed views, open passageways, etc). Moment frames overcome these limitations by providing brace-free spaces for passageways and unobstructed views, but can be limited by code pre-qualification restrictions which require orthogonal frame connections [AISC-358 (2010b)] (see Figure 3).
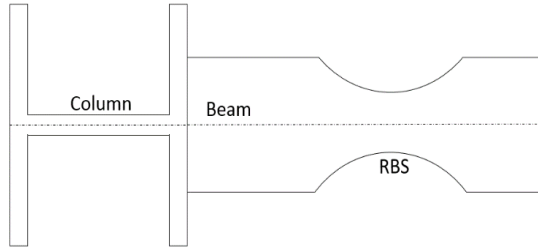
Figure 1 Plan view of beam-flange cuts in an RBS connection.
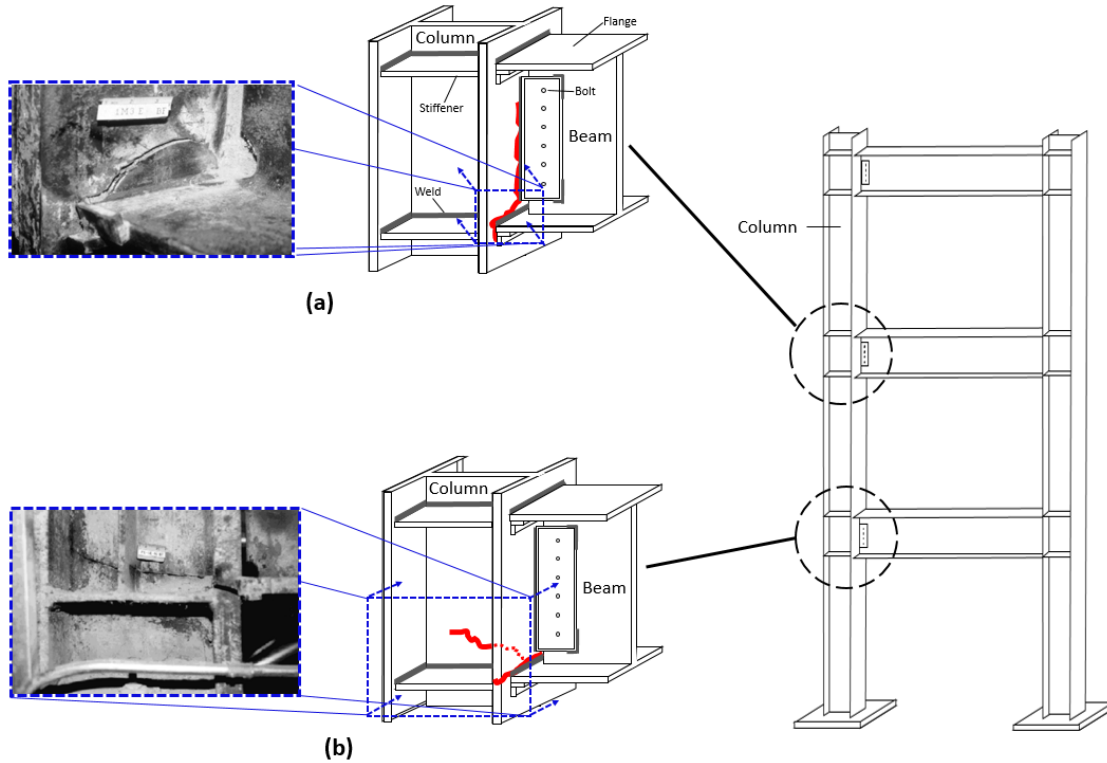
Figure 2 Common Post-Northridge Earthquake failure modes: **(a)** fracture of weld or column flange, **(b)** column flange rupture and propagation into column web. [ECA (2003)]
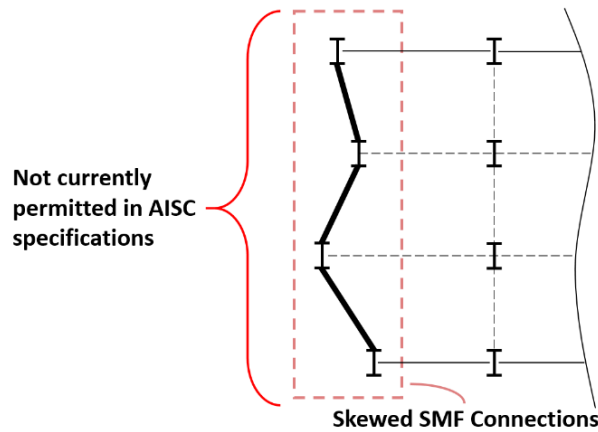
Figure 3 Example framing plan view of SMFs with skewed (non-orthogonal) connections.

Experimental testing and analytical investigations are required for pre-qualifying SMF connections. Existing prequalified RBS SMF connections in the Seismic Provisions for Structural Steel Buildings [AISC-358 (2010b)] are all orthogonal beam-column configurations [Hamburger et al. (2009)]. Information on seismic demands in skewed (non-orthogonal) RBS connections is limited.

In an effort to improve architectural flexibility of common moment frame configurations, Prinz and Richards (2016) investigated the performance of laterally skewed SMF connections with detailed finite element models. Two types of models were considered by Prinz and Richards (2016): one type simulating typical laboratory moment connection testing, and the other type more realistically representing building conditions (specifically column boundary conditions). Results demonstrated a complex relationship between out-of-plane skew, column twisting, column yielding, and strain demands in the RBS. Out-of-plane skew increased column twisting and resulted in irregular yielding in the column flange tips near the beam-to-column connections. While columns analyzed by Prinz and Richards (2016) contained some axial loads introduced through beam shear, effects of larger (more realistic) column axial loads on column twisting and the resulting system-level response are unknown.

Deep columns commonly used in SMF configurations can exhibit greater column twist than shallow columns due to the increased eccentricity from lateral movement of the RBS compression flange [Zhang and Ricles (2006), Chi and Uang (2002)]. Full-scale tests on un-skewed connection configurations [Zhang and Ricles (2006), Chi and Uang (2002)] were used to develop a procedure for predicting column torsion resulting from the use of RBS connections; however, it is not clear how large column axial loads combined with skewed RBS connections

3

will affect column torsional demands and the resulting beam bracing requirements.

The following research focuses on extending the work of Prinz and Richards (2016) by investigating effects from column axial loads on column twisting and yielding in skewed SMF RBS connections. The study involves advanced finite element modeling of SMF connections using techniques similar to Prinz and Richards (2016) and other analytical studies on SMF connections [Chi et al. (2006), Gilton and Uang (2002), Pachoumis et al. (2009), Zhang and Ricles (2006)]. The investigation consists of four out-of-plane beam skew angles of 0°, 10°, 20°, and 30° (see Figure 4); three column configurations representing shallow, medium, and deep columns; and four levels of column axial loads: 10%, 15%, 25%, and 50% of the nominal column compressive strength (ΦP_n).

In this thesis, a detailed description of the considered frame configurations is provided, modeling techniques are discussed, and results from the finite element analyses are presented. Following, conclusions on the effects of column axial loads in skewed RBS SMF connections are given.
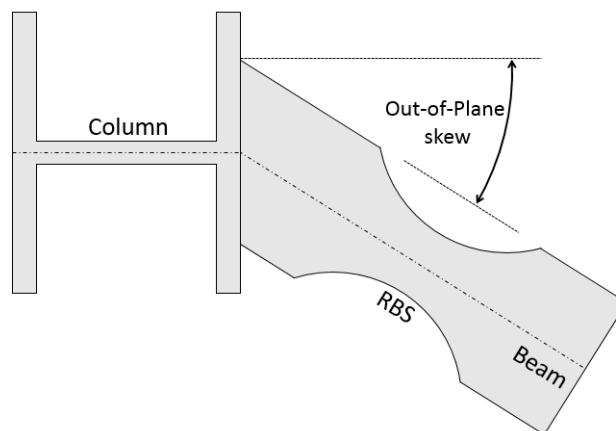
Figure 4 Plan view of out-of-plane (lateral) skew.

Frame Configurations

Three moment frame designs are considered in this study, consisting of shallow, medium, and deep-columns. The moment frame designs represent a three-story beam-column assembly (see Figure 5), which is different from traditional laboratory prequalification testing configurations. Traditional SMF assembly testing typically includes only one beam-column assembly spliced near the member inflection points; however, boundary effects from the column restraints in these configurations can be unrealistic and result in unrealistic column flexural demands. The three-story configuration used in this study allows realistic moment gradients and column torsional restraints to develop in the middle connection (termed 'Connection of Interest' (COI) in Figure 5). Similar three-story frame geometries were considered in the initial skewed SMF study by Prinz and Richards (2016).
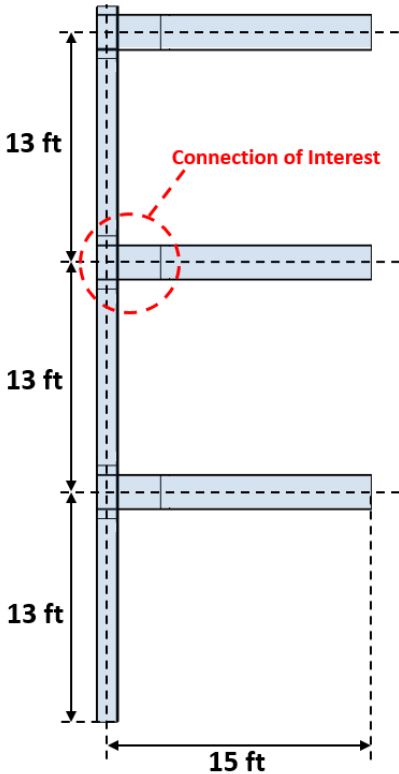
Figure 5 Model Geometry.

The considered beam-column configurations (presented in Table 1) are near the allowable slenderness limits provided in the AISC provisions [AISC (2010b)], representing worst-case skewed geometries for design. Also shown in Table 1 are the RBS flange cut dimensions ('a', 'b', and 'c', see Figure 6). Sample RBS flange-cut design calculations are presented later in Appendix C.

The deep column configurations in Table 1, while commonly used in un-skewed SMFs due to story drift and "strong-column/weak-beam" requirements [Hamburger et al. (2009)] create concerns about column twisting for skewed connections. Even in un-skewed geometries, the combination of lateral beam displacements (resulting from RBS-buckling) and out-of-plane column bending, often create higher warping stresses than more shallow columns. High "h/t_f^3" ratios are mainly responsible for large warping stresses in deep columns resulting from centerline distances between flanges (h) and flange thicknesses (t_f) [Chi and Uang (2002)]. Additionally, wider column sections, particularly the lighter-weight sections, are susceptible to local and lateral-torsional buckling [Hamburger et al. (2009)]. The column sections chosen in this study must also accommodate skewed beam geometry, which can result in wider required column flanges (see Figure 7).

The chosen SMF RBS connections incorporate both continuity plates and doubler plates for panel zone strength and ductility requirements (see Figure 8) [AISC (2010b)]. In addition, the continuity and doubler plates brace the column web and flanges to prevent local buckling in the connection.

Table 1 Beam-column combinations and the beam RBS flange-cut dimensions.

Column		Beam	Beam RBS dimensions (in.)		
			a	b	c
Shallow:	W14×132	W24×76	5.5	18	2
Medium:	W18×86	W24×76	5.5	18	2
Deep:	W30×173	W36×150	9	23	2.5

$$R = \text{Radius of Cut} = \frac{4c^2 + b^2}{8c}$$
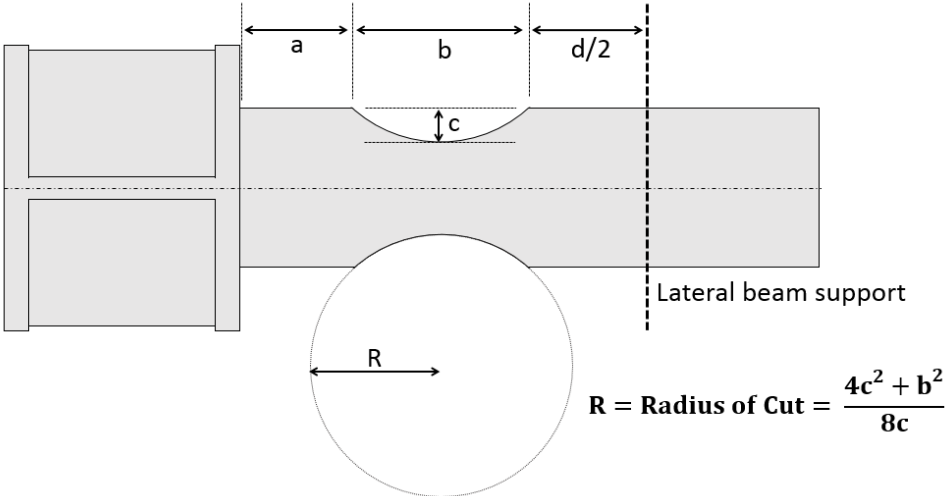
Figure 6 Reduced Beam Section details.

$$b_{0°} < b_{30°}$$
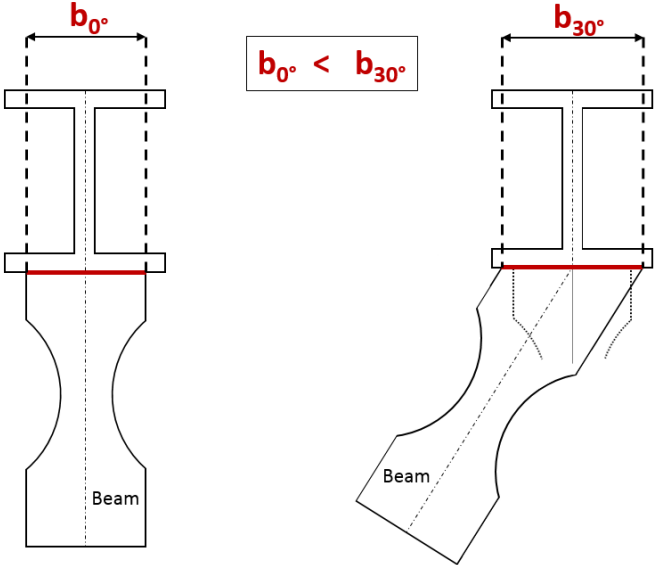
Figure 7 Increased column width "b" required by beam skew.
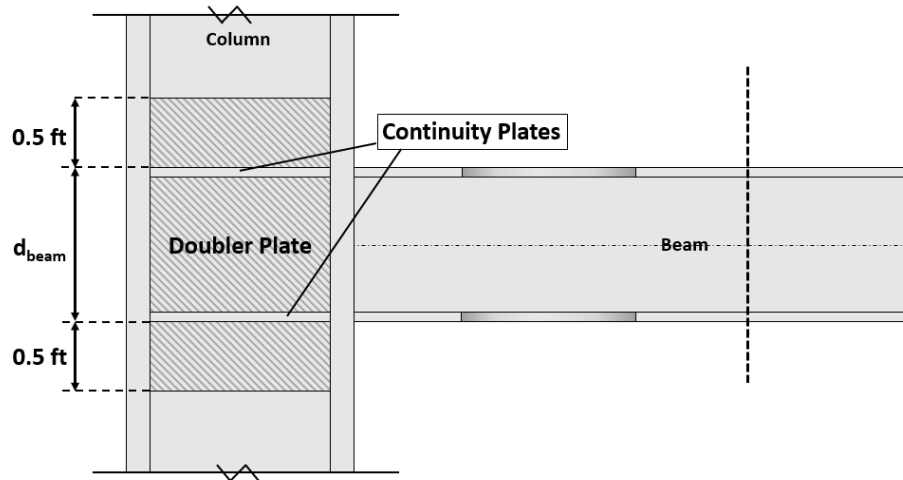
Figure 8 Connection Geometry.

2.1 Finite Element Modeling Techniques

A total of 48 advanced finite element simulations were performed, representing 3 beam-column configurations, 4 levels of beam skew, and 4 levels of column axial load. Table 2 presents the analysis matrix for the 48 simulations along with some results which will be discussed later in the 'Results and Discussion' section.

The finite element analysis software, ABAQUS/CAE [HKS (2006)], was used for all analyses. Shell elements (type "S4R" in ABAQUS) were used to model all frame geometries and are useful for simulating local buckling, asymmetric yielding, and generating local stress data for behavioral analysis at the connection. Reduced integration shell elements were used for computational efficiency and shear-locking prevention during the expected development of bending strains in the column and beam members, particularly in the RBS regions. The modeling methods used in this study are similar with those used in the previous study by Prinz and Richards (2016), allowing for comparison.

8

Table 2 Analysis matrix and results.

Model	Column	Beam	Beam Skew Angle (degrees)	Axial Compression Force (% of ΦP_n)	Peak Moment at Connection (K-ft)	Rotation at $0.8M_p$ (rad)	Column Twist at 0.04 rad drift (degrees)
W14X132_0_10%				10	869.19	0.053	0.102
W14X132_0_15%			0	15	872.02	0.053	0.093
W14X132_0_25%				25	862.24	0.053	0.096
W14X132_0_50%				50	868.77	0.054	0.081
W14X132_10_10%				10	857.14	0.050	0.194
W14X132_10_15%			10	15	856.40	0.051	0.193
W14X132_10_25%	W14X132	W24X76		25	857.34	0.051	0.186
W14X132_10_50%				50	853.46	0.052	0.247
W14X132_20_10%				10	857.98	0.050	0.259
W14X132_20_15%			20	15	855.65	0.050	0.260
W14X132_20_25%				25	852.89	0.050	0.268
W14X132_20_50%				50	850.33	0.052	0.428
W14X132_30_10%				10	851.97	0.049	0.318
W14X132_30_15%			30	15	854.16	0.050	0.326
W14X132_30_25%				25	852.89	0.050	0.354
W14X132_30_50%				50	846.82	0.052	0.670
W18X86_0_10%				10	874.22	0.051	0.184
W18X86_0_15%			0	15	875.54	0.051	0.193
W18X86_0_25%				25	866.17	0.051	0.214
W18X86_0_50%				50	873.32	0.052	0.041
W18X86_10_10%				10	855.35	0.050	0.402
W18X86_10_15%			10	15	855.69	0.050	0.421
W18X86_10_25%	W18X86	W24X76		25	855.09	0.051	0.453
W18X86_10_50%				50	853.29	0.052	0.587
W18X86_20_10%				10	832.89	0.050	0.643
W18X86_20_15%			20	15	831.69	0.051	0.692
W18X86_20_25%				25	832.97	0.051	0.773
W18X86_20_50%				50	837.94	0.051	0.821
W18X86_30_10%				10	817.91	0.051	1.102
W18X86_30_15%			30	15	817.88	0.052	1.137
W18X86_30_25%				25	817.76	0.052	1.117
W18X86_30_50%				50	819.12	0.050	0.730
W30X173_0_10%				10	2752.75	0.045	0.356
W30X173_0_15%			0	15	2738.61	0.044	0.392
W30X173_0_25%				25	2725.28	0.042	0.456
W30X173_0_50%				50	2747.22	0.037	-
W30X173_10_10%				10	2690.62	0.043	0.524
W30X173_10_15%			10	15	2693.11	0.043	0.566
W30X173_10_25%	W30X173	W36X150		25	2687.66	0.043	0.703
W30X173_10_50%				50	2691.69	0.038	-
W30X173_20_10%				10	2638.13	0.045	0.876
W30X173_20_15%			20	15	2637.68	0.045	0.977
W30X173_20_25%				25	2640.81	0.034	-
W30X173_20_50%				50	2640.81	0.035	-
W30X173_30_10%				10	2557.70	0.046	2.032
W30X173_30_15%			30	15	2557.92	0.046	1.993
W30X173_30_25%				25	2565.33	0.047	1.518
W30X173_30_50%				50	2571.84	0.038	-

A combined non-linear isotropic and kinematic material model defined the steel post-elastic strain hardening (see Eq.1) [ABAQUS (2015)]. The steel material plastic behavior used in the analyses was calibrated from stabilized cycles of A572 Gr 50 steel generated from cyclic coupon testing [Kaufmann et al. (2001)]. A572 Gr 50 steel is similar to A992 steel, commonly used in rolled wide-flange shapes within the United States.

$$\alpha = \frac{C}{\gamma}\left(1 - e^{-\gamma \varepsilon^{pl}}\right) + \alpha_1 e^{-\gamma \varepsilon^{pl}}$$
Eq. 1

The kinematic hardening parameter (C) and gamma 1 (γ) factor were 406.18 and 37.175, respectively. One backstress was used; therefore, α_1 was zero. Since large plastic strains were expected to develop in the analyses, a yield stress (ε^{pl}) of 63.5 Ksi was specified to fit the hardening model to the backbone curve at larger strains, allowing better hardening accuracy during large plastic straining which was to be expected during the analyses. Figure 9 shows the calibrated hardening model (blue) in comparison with the backbone curve (red) derived from the stabilized cyclic coupon test data for A572 Gr 50 steel up to 8% strain [Kaufmann et al. (2001)]. Previous finite-element investigations [Richards and Prinz (2007), Prinz and Richards (2016), Richards and Uang (2005)] have used this plastic strain data in their models, which produced realistic global plastic strain responses for A992 steel.

The degrees of freedom (DOFs) shown in Figure 10 are chosen to represent realistic constraints for the interior moment frame connection. The DOFs at the column's base represent a pinned connection, conservatively overestimating connection flexural demands and first-story drift [Hamburger et al. (2009)]. Lateral beam supports restrain lateral movement of

the buckled RBS, and placed at the maximum allowable spacing of half the beam depth away

from the RBS.
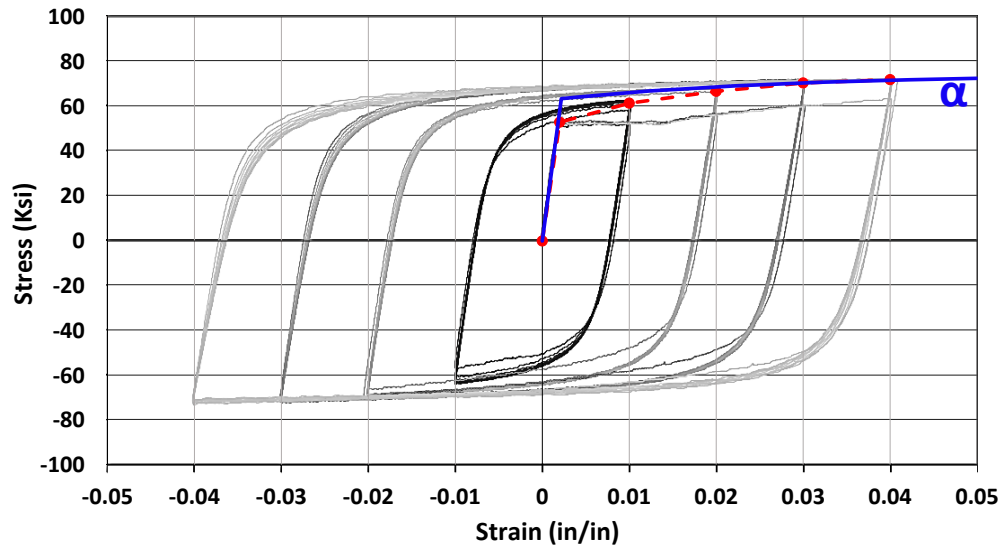
Figure 9 Comparison of backbone curve and the hardening model [Kaufmann et al. (2001)].

All DOFs at a given location were applied to a node located at the cross section's

centroid. These particular nodes are constrained (or rigidly tied) to all edges within its cross-

section, which allows the applied boundary conditions to behave uniformly across the entire

cross-section. Prinz and Richards (2016) considered similar boundary conditions, with the

exception of column base fixity.
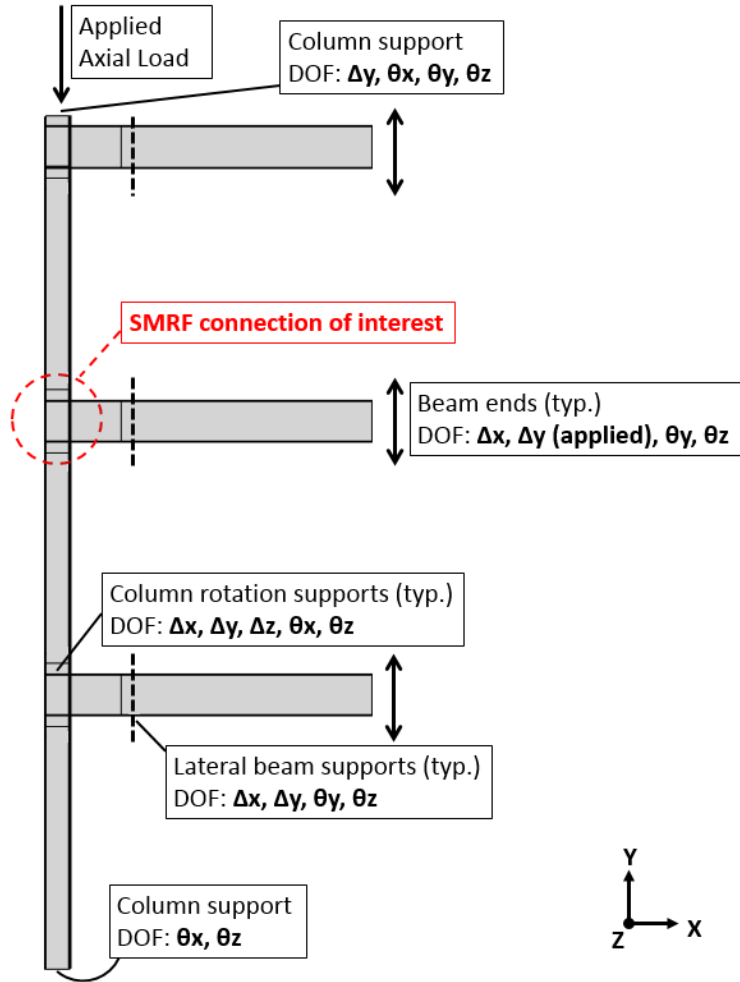
Figure 10 DOFs and applied loads**.**

2.2 Mesh Size and Initial Imperfections

For computational efficiency, the mesh size varied between 0.5-inches in the connection regions to 2.0-inches outside of the connection regions (see Figure 11). Larger mesh sizes were used outside the connection regions where an elastic response and low strain gradients are expected. Finer mesh sizes are used within the connection regions for better accuracy in areas of non-uniform geometry and high expected plastic strain gradients. The chosen refined mesh size of 0.5-inches corresponds to that used by previous studies of finite-element analysis of RBS moment connections [Zhang and Ricles (2006)], which achieved reasonable results.

12

To simulate fabrication tolerances, present in actual construction, initial imperfections were applied to all simulated geometries. These initial imperfections were scaled from the buckled mode shapes determined from eigen-frequency analyses. Frequencies for the twelve different model geometries were obtained using linear perturbation analysis in ABAQUS (see Figure 12). Mode-shapes were then superimposed on the models as initial deformations, and scaled by the straightness tolerance limit of "L/1000" [AISC (2010a)], where L is the column's unbraced length.
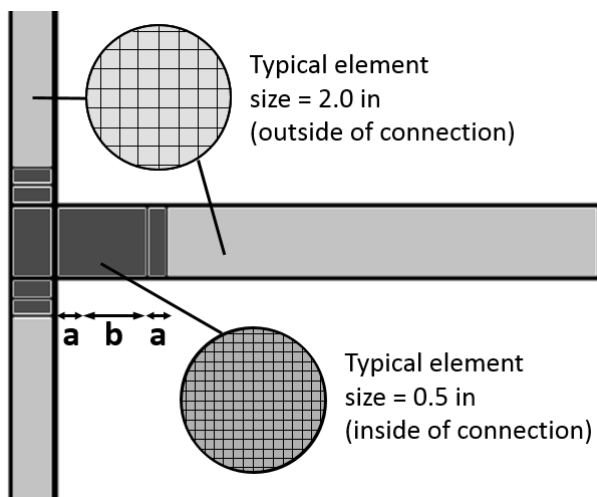
Figure 11 Overview of meshing with locations of refinement.
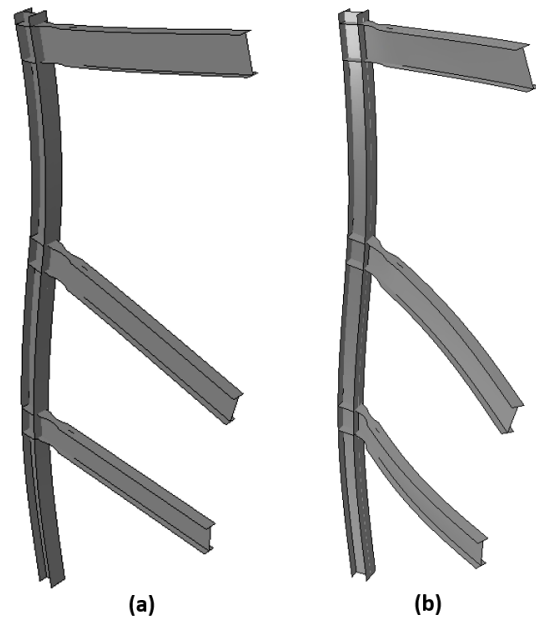
Figure 12 Fundamental frequency mode shapes for W14X132 models with **(a)** 0° skew, and **(b)** 30° skew. Note the deformed shapes are scaled by 50 times for ease of viewing.

2.3 Loading Protocol

All columns are loaded with an axial load equal to a percentage (between 10% and 50%) of the nominal compressive strength (ΦP_n). Because the columns in SMFs are often sized based on drift limits and ultimate demands from the RBS regions, column sections are often much larger than those required for gravity loads alone, and axial compressive loads up to 50% ΦP_n represent fairly large axial loads. Additionally, the columns used in this study are close to the slenderness limits for members in axial compression, again representing worst-case design scenarios. The slenderness limits for members with axial compression specified in AISC steel construction manual (2011) outline the calculation for member nominal compressive strength (see Appendix D for determining the nominal compressive strengths, ΦP_n).

All models were loaded using the displacement-based protocol (see Figure 13) specified in AISC seismic provisions (2010b). This loading protocol has been used in both analytical and full-scale testing of SMF components [Tsai et al. (1995), Chi and Uang (2002)]. The protocol outlines the number of cycles and the applied interstory drift. In this study, beam-end deformations (Δ_y) were used to apply connection interstory drift rotations.

Acceptable ductility for connection prequalification is defined as having reached and completed two cycles at 0.04 rad storydrift [AISC-341 (2010b)] (see Figure 13). The loading protocol continued to 0.08 rad drift (two cycles per +0.01 rad increments, as specified in the AISC seismic provisions (2010b)) to investigate the behavior of the SMFs at extreme deformations and determine the capacity of the connections.

The nonlinear geometry option in ABAQUS captured large displacement effects on the SMF assembly by considering the orientation of individual elements and the resulting

14

component forces. Note however, that the analyses performed are insufficient for capturing

crack initiation or propagation, which would typically occur at larger strains and influence the

behavior of the assembly. Such cracks are unexpected within the connections due to the

stiffening modifications (continuity plates and doubler plate).
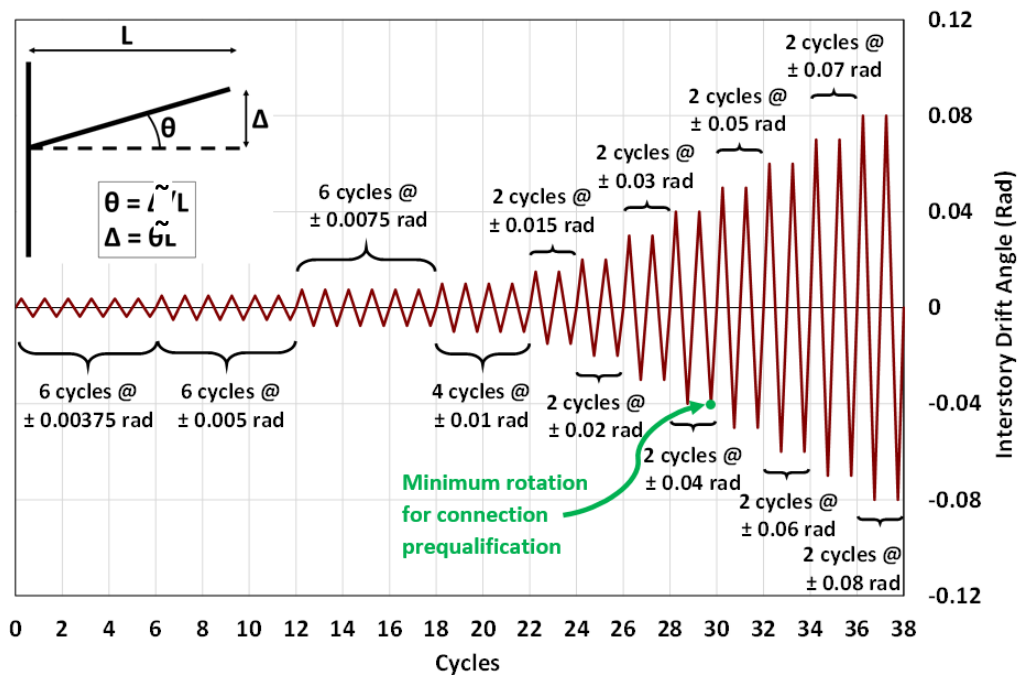
Figure 13 Loading protocol.

3. Results and Discussion

3.1 Effect of Column Axial Loads on Global Connection Response (Yielding and Buckling)

Column axial loads (P) affect the resulting lateral displacements (Δ) and can increase the

presence of local buckling. Increasing axial load causes amplification of flexural/lateral

displacements leading to column local buckling. In addition, skewed beam-column connection

geometries force the columns to resist moments with both strong and weak axes (see Figure

14) causing in-plane (strong axis, Δ_x) and out-of-plane (weak axis, Δ_y) bending in the columns.

15

The distribution of accumulated equivalent plastic strain (PEEQ in ABAQUS) within the connection of interest (COI) showed little change with increasing axial loads (see Figure 15). Increase in column-flange yielding between the 25% and 50% ΦP_n in the shallow-column SMFs was attributed to initiation of column local buckling, since the SMF eventually buckled below the COI (second-story connection) (see Figure 16a). Most medium-column SMFs and all deep-column SMFs experienced column local buckling below the first-story connection (see Figure 16b), and therefore showed no noticeable increase in PEEQ distribution in the column-flange at the COI.

"Reactionary moments" at the column-flange were calculated by multiplying the reactionary vertical force at the beam-end and the moment arm (the beam length) (see Figure 17). Reactionary moments obtained at multiple storydrifts (0.02, 0.03, 0.04, and 0.05 rad drift) determine the SMF connection performance and help visualize RBS buckling and identify the development of instability mechanisms within the SMFs. Since the beam-column configurations narrowly satisfy slenderness limits, the SMF "moment capacities" (reactionary moments following the development of an instability mechanism) were limited by column local buckling at relatively large drifts. The column properties for the three SMF combinations (see Table 3) are used to relate and compare the overall performance of the three SMFs.
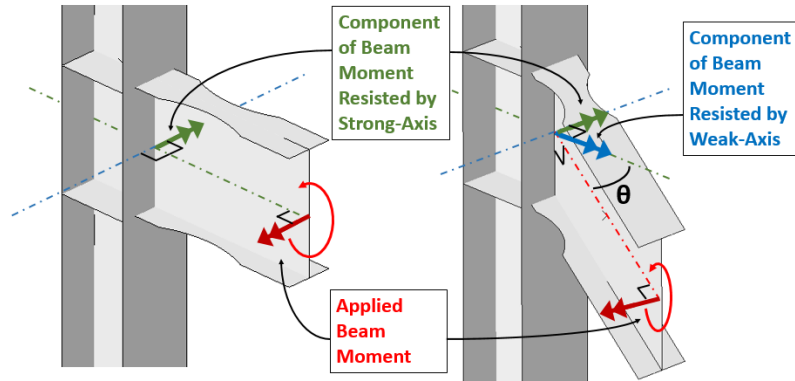
Figure 14 Resisting of moment forces by the strong and weak axes of the column due to beam-skew.
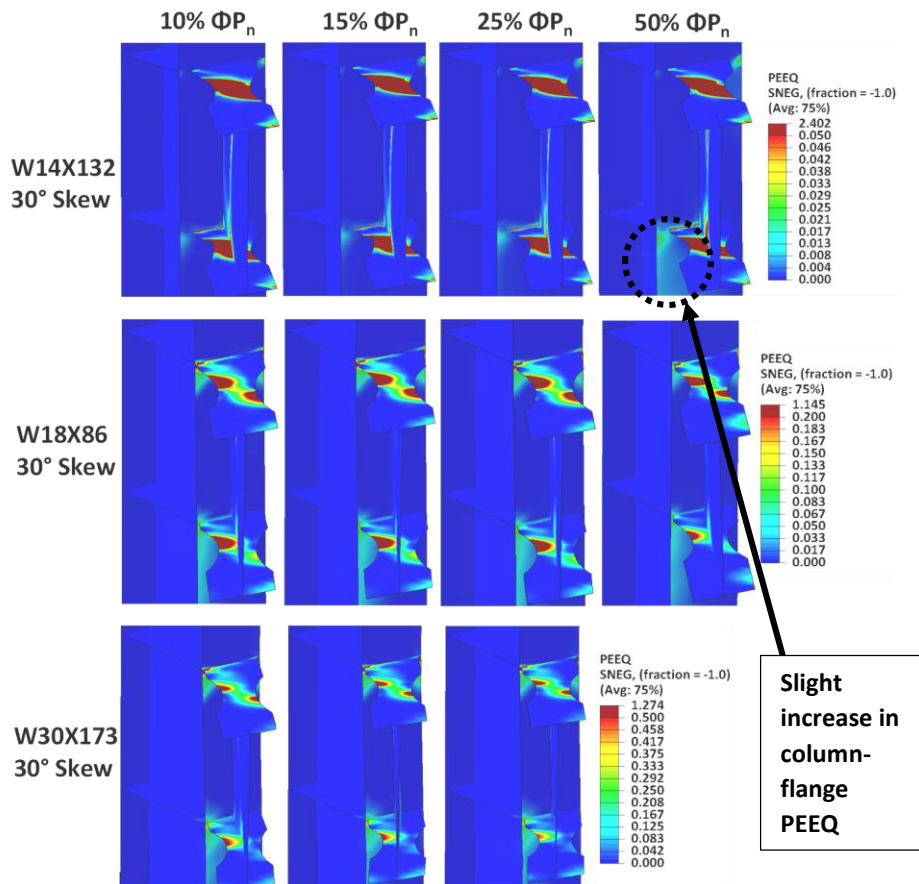
Figure 15 Effect of column axial loads on PEEQ distribution in the COI at 0.04 rad drift, for models with 30° skew. Note the deep-column SMF connection at 50% ΦP_n failed before reaching 0.04 rad drift.
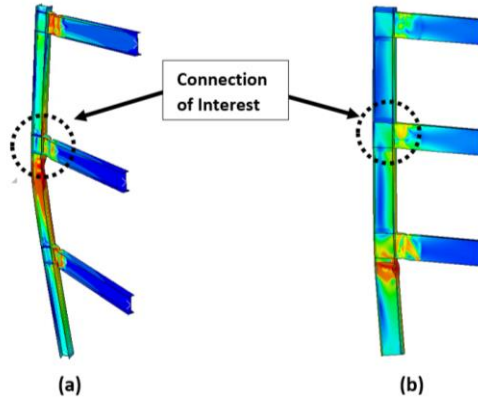
Figure 16 Failure from column local buckling below the: **(a)** second-story connection for the shallow column model with 30° skew and 50% ΦP_n; **(b)** first-story connection for the deep column model with 20° skew and 25% ΦP_n.
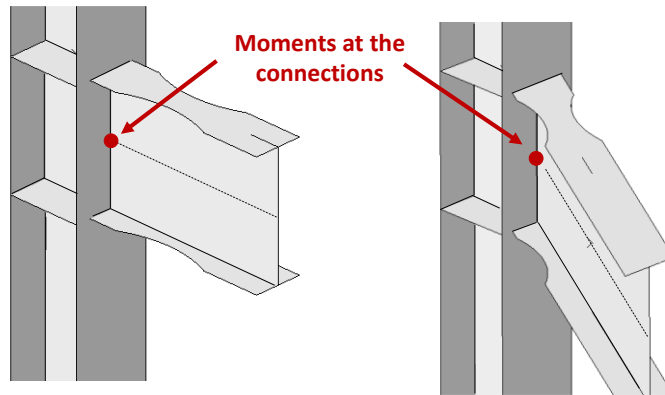
Figure 17 Location of connection-moment data.

Table 3 Column properties.

	W14×132 (shallow)	W18×86 (medium)	W30×173 (deep)
ΦMp_x (K-ft)	878	698	2280
ΦMp_y (K-ft)	424	182	461
J (in^4)	12.3	4.1	15.6

3.1.1 Shallow-Column Models (W14×132)

The shallow-column (W14×132) SMF simulations demonstrated the most ductility, when compared to the medium and deep column SMFs. Reactionary moments at the connection

initially increased in early interstory drift cycles, but decreased after 0.03 rad drift due to the

RBS buckling and loss of bending strength (see Figure 18). Level lines in early story drifts

indicate the beam-skew having almost no effect on the shallow-column SMFs' reactionary

moment. Eventually, asymmetric load distribution induced by beam-skew began to negatively-

influence the reactionary moments in later story drifts (0.05 rad drift) as distributed yielding

within the connection increased.

    Figure 18 shows the relationship between beam skew, and moment capacity for various

levels of column axial load. With the exception of the largest axial load, it is evident that axial

load has little effect on the skewed SMF moment capacity (compare the plots in Figure 18). The

decrease in moment capacity for the 50% ΦP_n axial load, 30deg skew, at 0.05rad drift can be

attributed to increased yielding of the column compression flange below the second-story

connection, leading to column local buckling initiation (see again Figure 16a).
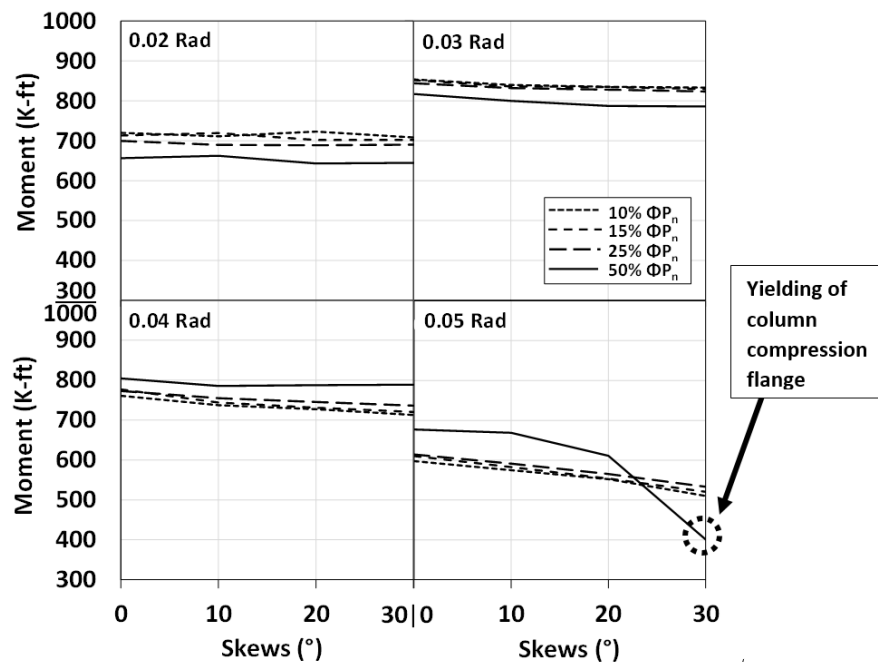
Figure 18 Effects of beam-skews and axial loads on reactionary moments at the connection for shallow-column SMFs at various interstory drift angles.

19

3.1.2 Medium-Column Models (W18×86)

Moment capacities in the medium-column (W18×86) SMF connections were similar to those in shallow-column SMFs; however, the downward trend in moment capacity with increased skew angle at early story drifts indicates a negative-influence of beam-skew on resulting moment capacity. These downward trends gradually level-out in larger story drifts (story drifts greater than 0.03rad). Note that the similarities in performance between the medium and shallow column could be attributed to the configuration, wherein the same beam section was used.

Much like the shallow-column models, moment capacities for the lowest axial loads (ΦP_n between 10%-25%) are grouped close to one another indicating a negligible influence of column axial load on global connection performance (see Figure 19). However, the highest column axial load (50% ΦP_n) resulted in initiation of column local buckling and subsequent decrease in SMF moment capacity (see again Figure 19). Column local buckling was observed near the first story connection for the 20° and 30° skewed connections at 0.04rad story drift (see Figure 19a) and near the second story connection at 0.05rad drift for the 0° and 10° beam-skews (see Figure 19b and Figure 19c). The differing column local buckling locations illustrates the level of influence beam-skew exhibits on the global behavior of the SMFs with 50% ΦP_n.
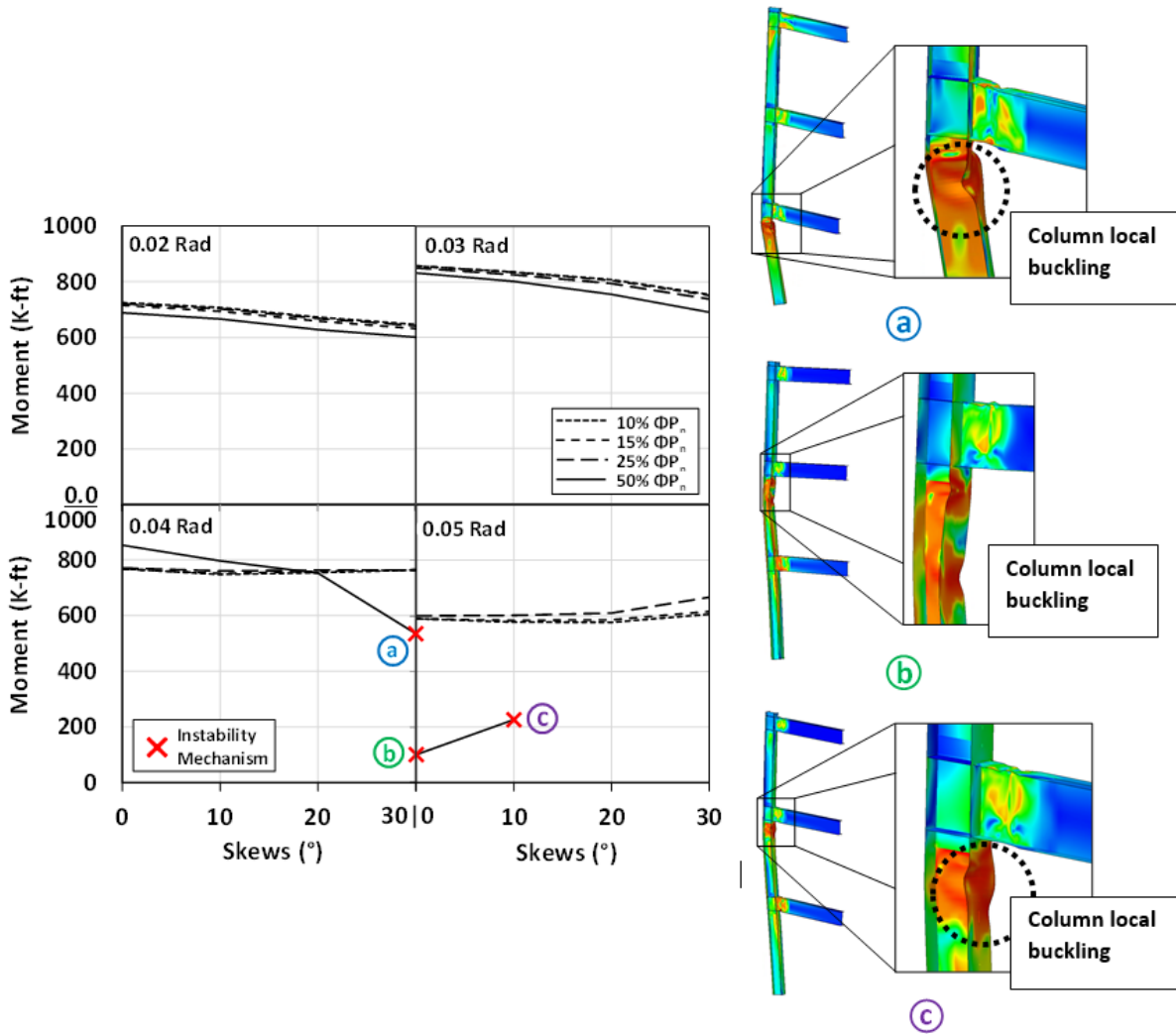
Figure 19 Effect of beam-skews and axial loads on connection moment capacity for medium-column SMFs at various interstory drift angles. Also included are the visualizations of the instability mechanisms.

3.1.3 Deep-Column Models (W30×173)

The deep-column (W30×173) SMFs, which have the greatest overall flexural capacities, performed the worst during cyclic loading due to column local buckling issues (see Figure 20). Many of the deep-column SMF simulations experienced column local buckling at low connection rotations (near 0.03rad). Due to these early local buckling issues at higher axial loads, connection moment capacities from only the two lowest axial loads (10% and 15% ΦP_n) are valid for determining the effects of beam-skew and axial load on connection response. As

21

shown in Figure 20, increased beam skew results in a slight reduction in moment capacity;

however, the addition of moderate axial loads (between 10% and 15% ΦP_n) appears to have

negligible effect on connection performance (note in Figure 20 that the resulting moment

capacity from the 10%-15% ΦP_n axial loads are tightly grouped at all skew levels). Under higher

axial loads (25% and 50% ΦP_n), the SMF connections were negatively affected by increased

beam skew (see Figure 20). Under 50% ΦP_n column axial load local buckling initiated at 0.03rad

for all levels of beam skew. Under the 25% ΦP_n column axial load, local buckling initiated at

0.03rad for connection skews of 20 and greater.

These observations raise concerns for the justifications behind modern approach of

using deeper column sections in SMFs. These tests relied on the ductility of all components

(beam, column, and the connection) to achieve the adequate level of ductility of 0.04 rad drift

[AISC 341 (2010b)]. The deepest/stiffest column and beam sections significantly reduced the

frame's overall ductility. Given the sudden failures of the deep-column SMFs with moderate to

high axial loads (25% to 50% ΦP_n) (see Table 4); imprecise axial load estimations could lead to a

substantial reduction in ductility through premature column local buckling. For the deep-

column SMFs, simply increasing the axial load from 25% to 50% ΦP_n affects whether the frame

achieves the 0.04 rad drift or not, regardless of beam-skew. The early column local buckling

observed coincides with the failure mechanisms observed in the full-scale experiments on deep

columns subjected to both axial loads and strong-axis bending [Uang et al. (2017)].
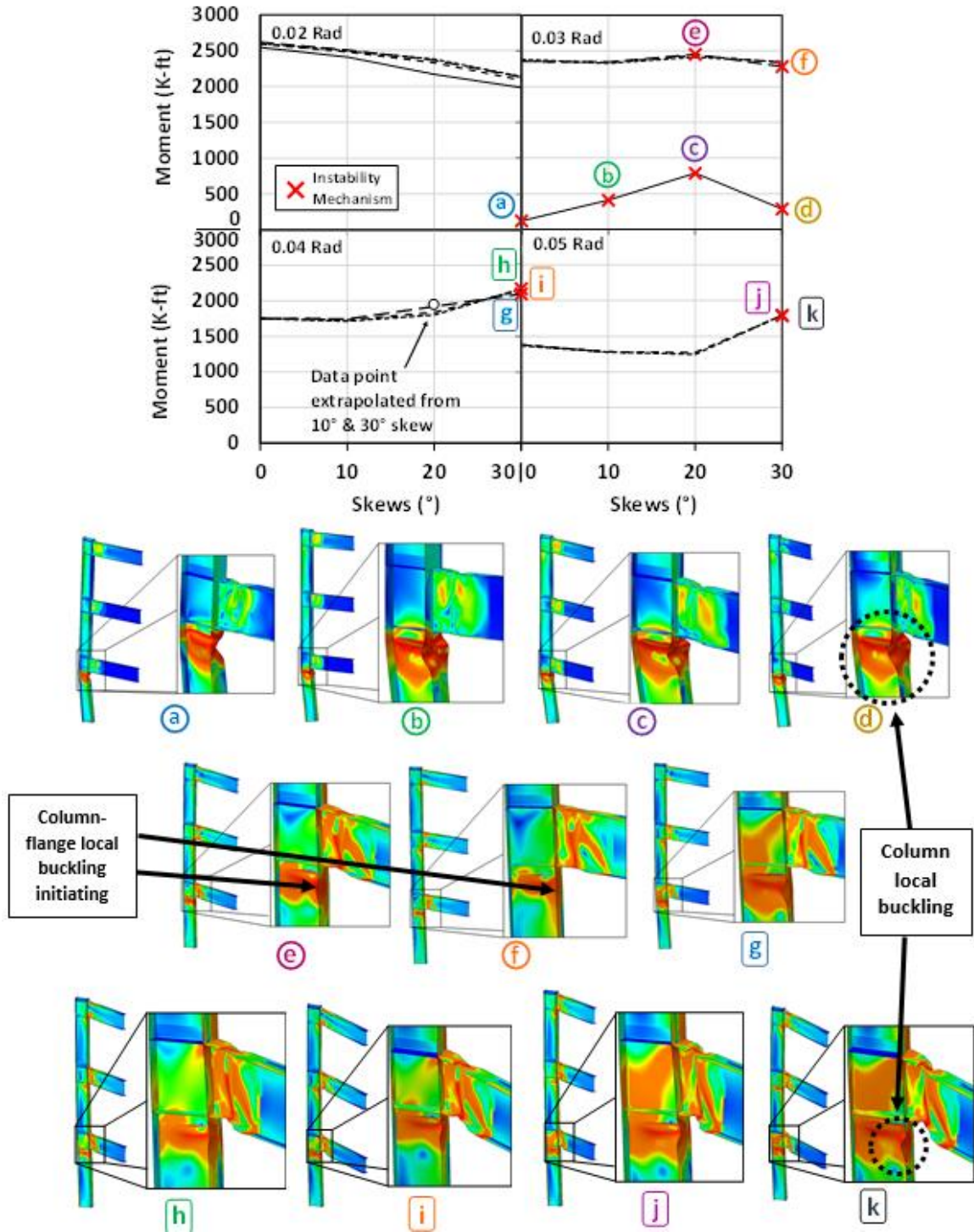
Figure 20 Effect of beam-skews and axial loads on reactionary moments at the connection for deep-column SMFs at various interstory drift angles. The missing data point (20° skew, and 25% ΦP_n) is due to column buckling prior to completing 0.04 rad drift, as shown in Figure 16b, and an explanation is given in section 3.2.3. Also included are the instability mechanism visualizations, where points "h", "i" and "j", "k" are 10% and 15% ΦP_n, respectively.

Table 4 *Deep-column SMF failure observations.*

Model	Rotation of Column Local Buckling Initiating (rad)
W30×173_0_10%	-
W30×173_10_10%	-
W30×173_20_10%	-
W30×173_30_10%	First cycle of 0.04
W30×173_0_15%	-
W30×173_10_15%	-
W30×173_20_15%	-
W30×173_30_15%	First cycle of 0.04
W30×173_0_25%	-
W30×173_10_25%	-
W30×173_20_25%	First cycle of 0.03 *
W30×173_30_25%	First cycle of 0.04 *
W30×173_0_50%	First cycle of 0.03 *
W30×173_10_50%	First cycle of 0.03 *
W30×173_20_50%	First cycle of 0.03 *
W30×173_30_50%	First cycle of 0.03 *

* Model failed (column local buckling) in first cycle of subsequent rotation.

3.2 Effect of Column Axial Load on Skewed RBS Connection Column Twisting

Out-of-plane skew increased out-of-plane bending and resulted in increased column twisting and column flange tip yielding near the beam-to-column connections similar to the findings from [Prinz and Richards (2016)]. The beam-skew resulted in beam moment components along both the strong and weak axes of the column, which led to the development of torsional forces (T_{skew}) within the column section (see Figure 21a).

Equivalent plastic strain (PEEQ) in the column-flange at the connection increased as the skew angle increased (see Figure 22), resulting from asymmetric yielding of the RBS, which ultimately led to larger lateral RBS displacements. However, the lateral displacement of the buckled RBS caused additional torsion within the connection (T_{RBS}) (see Figure 21b). The torsion

in the column resulting from lateral movement of the RBS resembled the torsion induced by beam-skew, since they were both derived from the same beam-flange force (F). Therefore, the total torsion from both mechanisms (skew and RBS deformations) can determined by combining the various force-eccentricity pairs.

Lower column axial loads (between 10% to 15% ΦP_n) had little effect on resulting column twist (see Figure 23); however, the moderate axial load (25% ΦP_n) caused premature column local buckling in the deep-column SMFs at 20° and 30° skews. The highest axial load (50% ΦP_n) caused early column local buckling in the medium-column SMFs at 30° skew and complete column instability for the deep-column SMFs prior to reaching 0.04rad drift. Further discussion on the performance of each column depth configuration is provided in the following sections.

$$T_{skew} = F (e_{x\text{-}skew}\cos\theta + e_{y\text{-}skew}\sin\theta)$$

(a)

$$T_{RBS} = F (e_{x\text{-}RBS}\cos\Phi + e_{y\text{-}RBS}\sin\Phi)$$

(b)
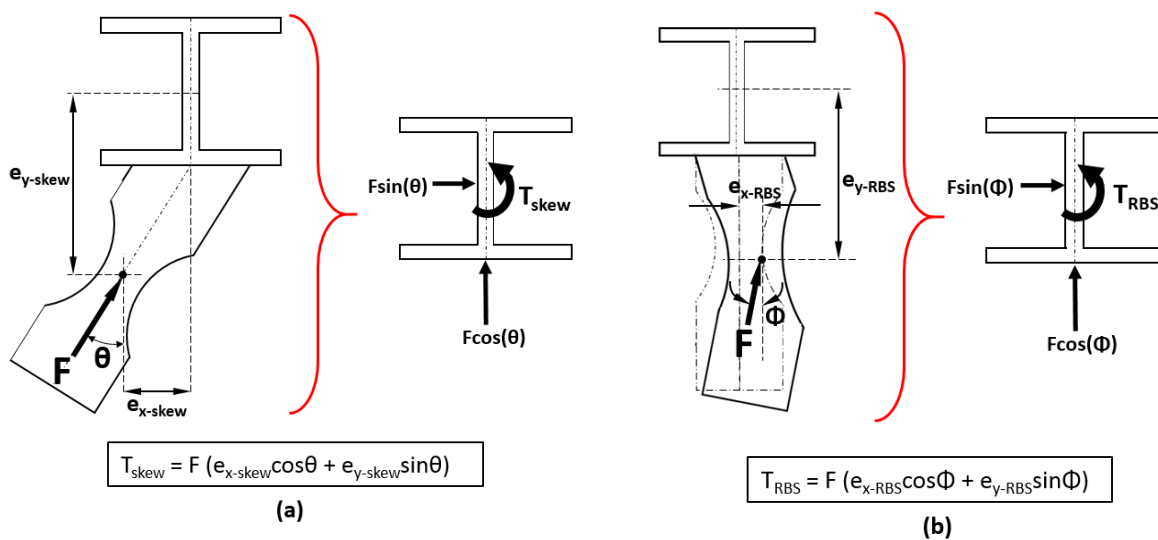
Figure 21 Column torsion and weak axis bending produced by **(a)** out-of-plane beam skew and **(b)** lateral-torsional buckling of the RBS [Chi and Uang (2002)].
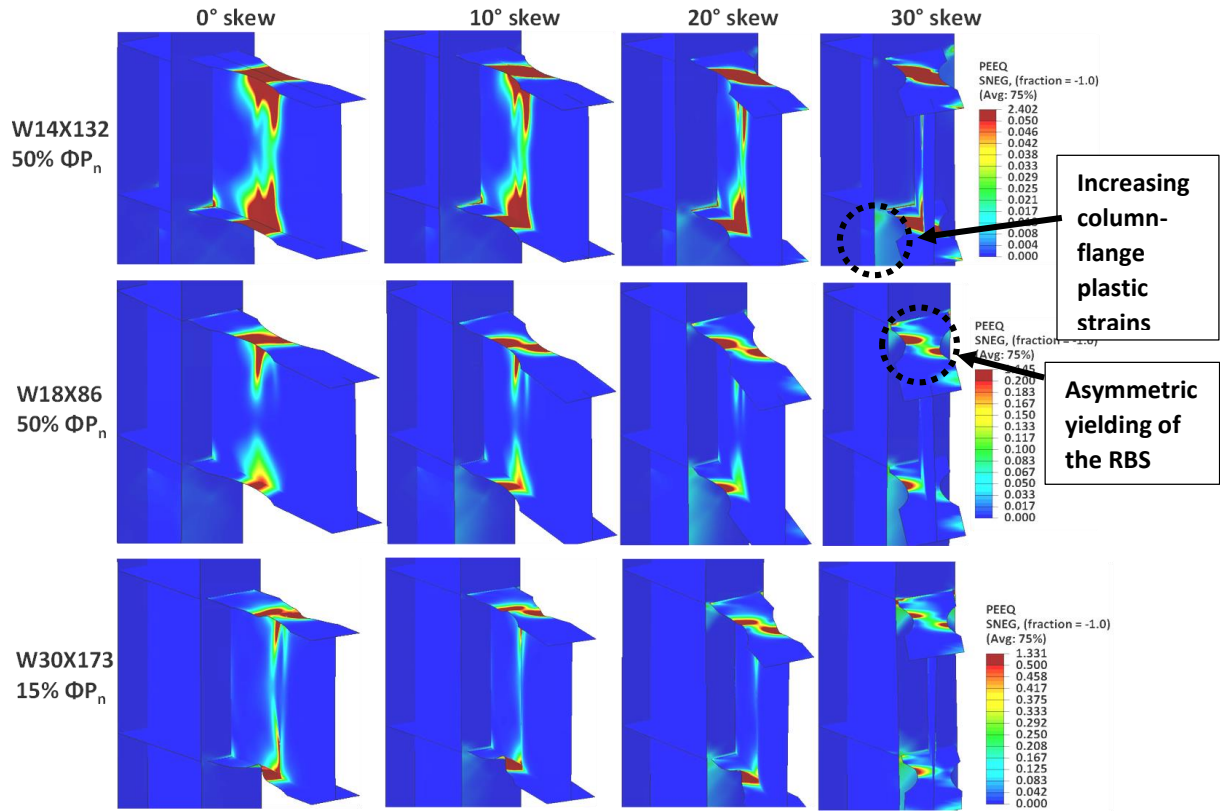
Figure 22 Effect of beam-skew on equivalent plastic strain (PEEQ) distribution in the COI at 0.04 rad drift, for SMFs with a consistent axial load.
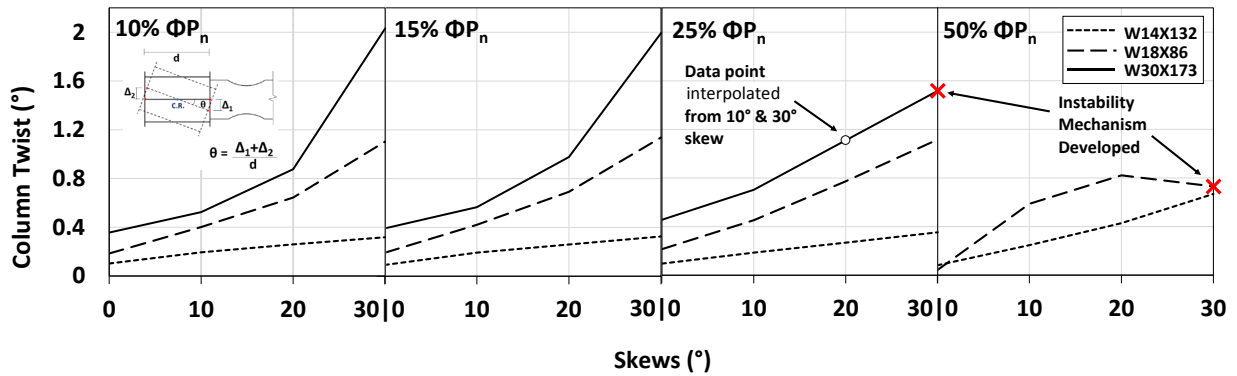
Figure 23 Effect of beam-skew and axial load on column twist at 0.04 rad drift.

3.2.1 Shallow-Column Models

The shallow-column section (W14×132) experienced the lowest column twisting of the three beam-column configurations (see again Figure 23). Beam-skew showed a consistent correlation with column twist in all SMFs, which was expected due to the torsional force resulting from the out-of-plane moment components.

Increased axial loads, excepting the highest axial load that led to column local buckling at high drifts, had a negligible effect on column twisting. Note in Figure 24 that the column twist behavior from the 10%-25%ΦP_n axial loads are tightly grouped at all beam-skew levels. Under larger column axial loads (50% ΦP_n), the columns experienced local buckling, but only in later storydrifts (0.06 rad drift). No column local buckling was observed in any of the shallow-column SMFs leading up to 0.05 rad drift. All of the column twist data were calculated from flange displacements Δ_1 and Δ_2 as shown in Figure 25.

Axial-loads and beam-skews are inherently tied to column twisting, since they both influence the development of axial, torsional, and flexural stresses in the columns; however, any deleterious effects of combining axial load and beam-skew are only evident under the largest axial load (note the increase in column twist of the 50% ΦP_n line in Figure 24).
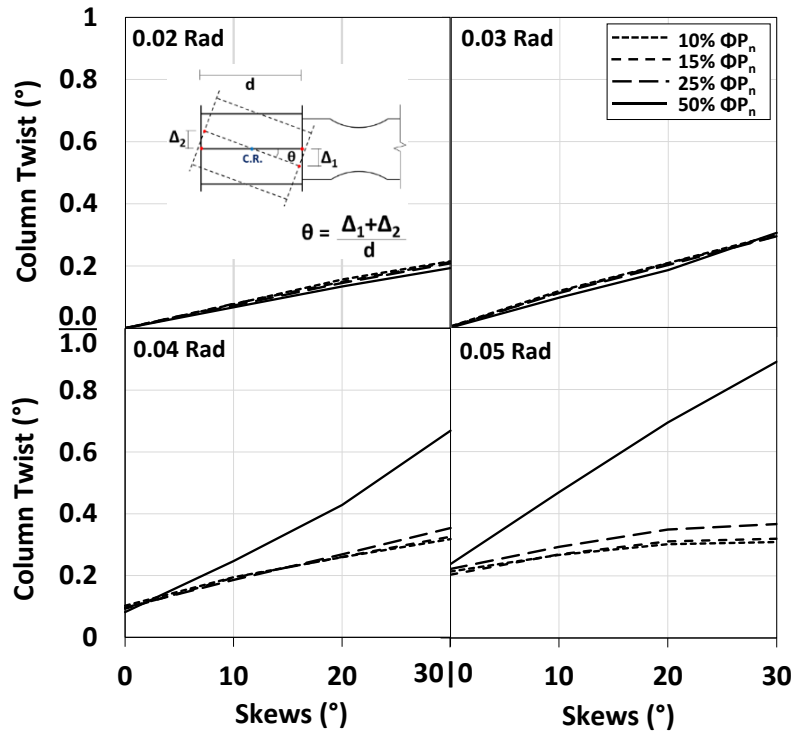
Figure 24 Column twist with differing skews and axial loads for the shallow-column SMFs at various interstory drift angles.
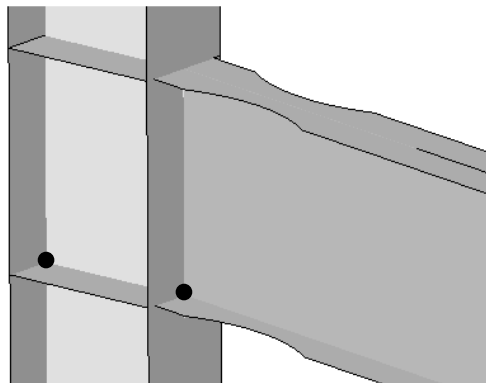
Figure 25 Location of data points for obtaining column twist.

3.2.2   Medium-Column Models

The medium-column (W18X86) SMFs exhibited less ductility than the shallow-column

(W14X132) SMFs. Because the beam sections remained the same between the shallow and

medium-column SMFs, the increased column twist can be attributed to both the lower column

28

polar moment of inertia and deeper section, which led to decreased torsional stiffness and higher eccentricity (e_{y-skew}) from beam skew (see again Figure 21a) when compared to the shallow column section.

Beam-skew influenced the magnitude of plastic strains experienced in the column web and flanges below the first and second-story connections, and was demonstrated by the differing location of column local buckling in the SMFs with the highest axial load. Beam-skew showed a strong correlation with column twist and resembled the shallow-column SMFs, where increase in beam-skew subsequently increased column twist (see Figure 26).

Increased column axial loads had a negligible effect on column twist, at rotations up to 0.04rad. Figure 26 shows the relationship between beam-skew angle, column twist, and applied axial load. Note in Figure 26 that axial load effects begin to increase the amount of column twisting at high connection rotations (0.05rad and greater). The column of the 50% ΦP_n load case experienced local buckling, which reduced column twist similar to the way a soft-story reduces interstory drifts at subsequent floors.

3.2.3   Deep-Column Models

The SMFs containing deep columns (W30×173) demonstrated the highest overall column twist (see Figure 27). Beam-skew increased column twist, but determining the contribution at the COI is limited since the early development of column local buckling below the first-story connection relieved some torsional stresses. The effect of the two lowest axial loads (10% and 15% ΦP_n) on column twist indicate negligible effects of axial load on resulting column twist (see Figure 27).

29
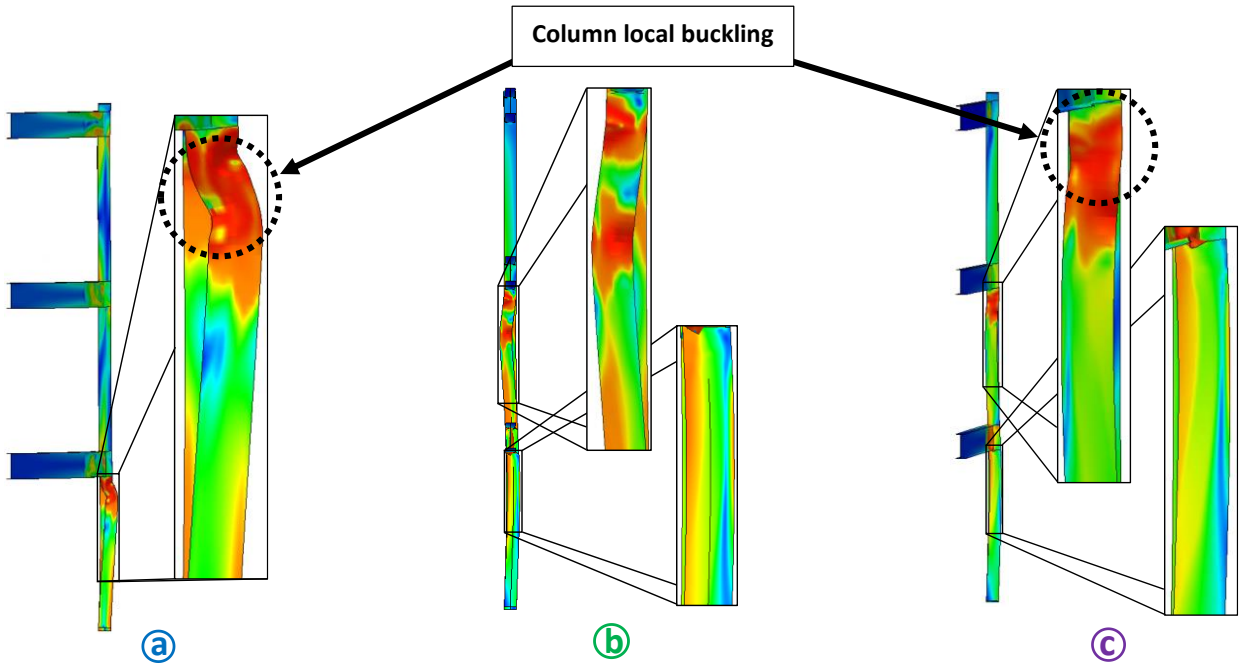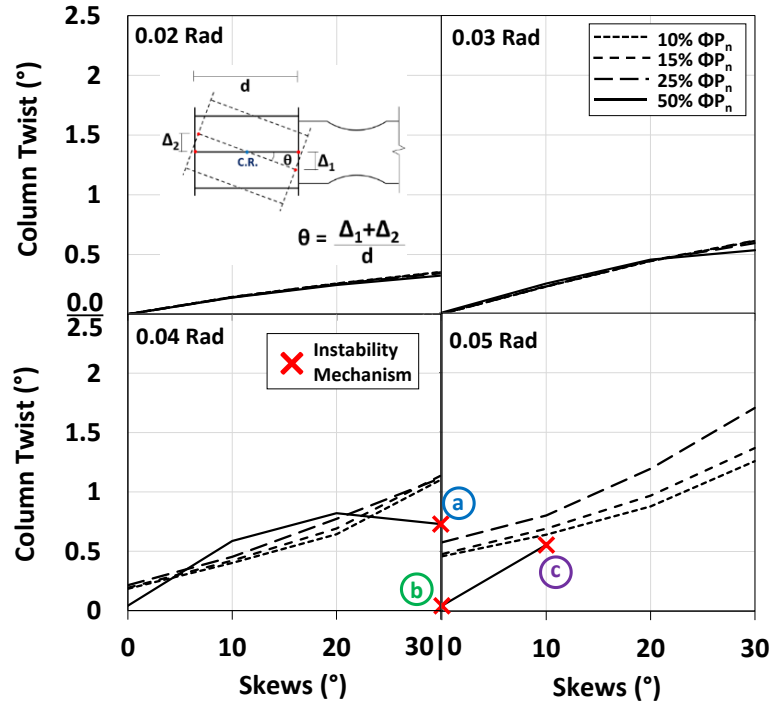
Figure 26 Column twist with differing skews and axial loads for the medium-column SMFs at various interstory drift angles. Also included are the instability mechanism visualizations of the column compression flange.
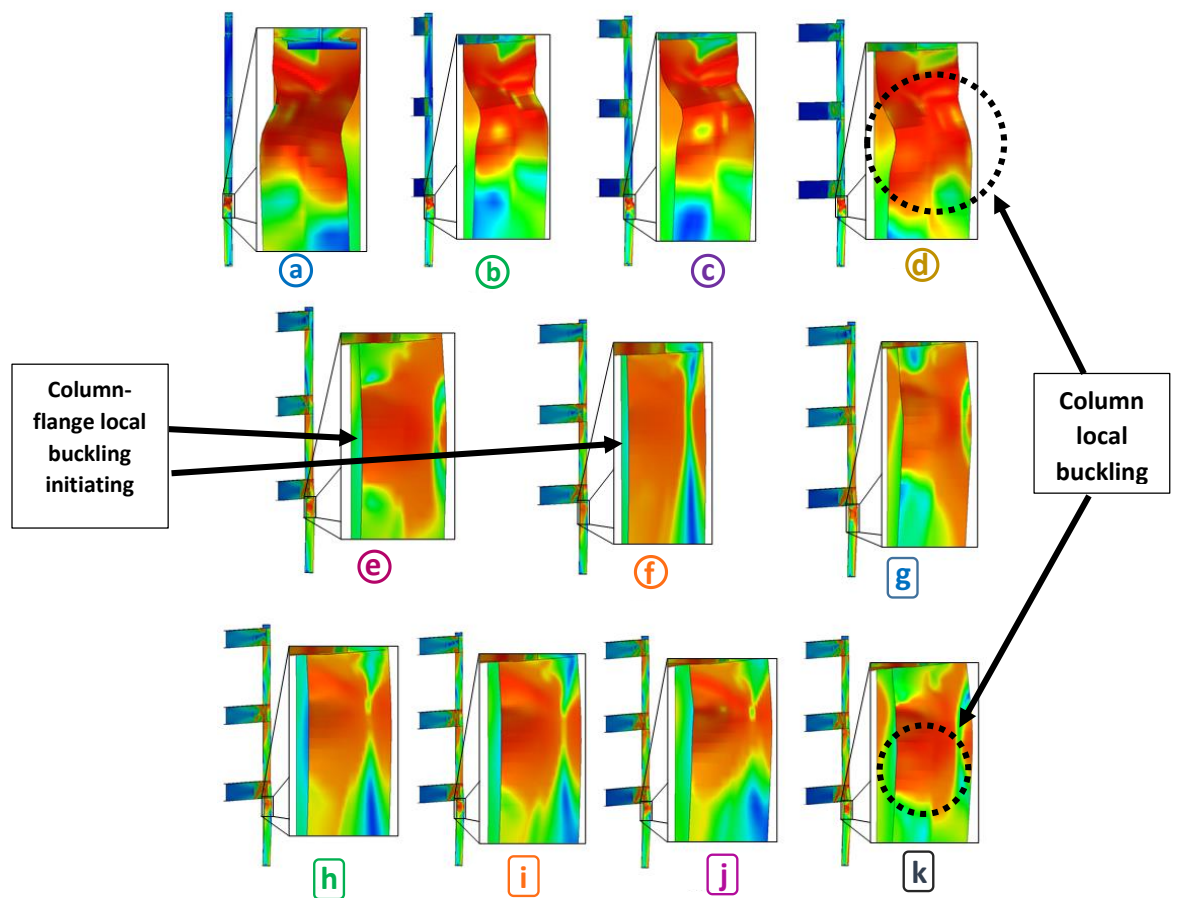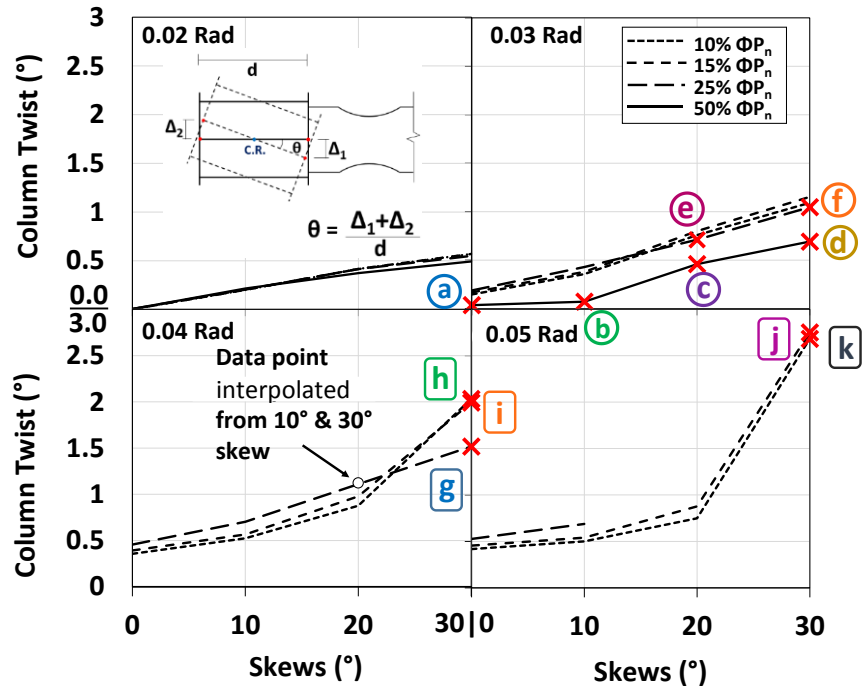
Figure 27 Column twist with differing skews and axial loads for the deep-column SMFs at various interstory drift angles. Also included are the instability mechanism visualization of the column compression flange.

3.3 Column Flange Stress

Column-flange equivalent plastic strains (PEEQ in ABAQUS) were obtained to investigate the distribution of yielding within the connection at differing beam-skews and axial loads. Plastic strain data was obtained at two locations: 1) the column flange-tip outside the beam-to-column connection and 2) the lower beam-to-column flange connection where fractures were observed following the 1994 Northridge Earthquake (see Figure 28).

The column flange-tip consistently experienced the greatest amount of plastic strains. The plastic strains resulted from the applied boundary conditions to the column cross section at that location which restricted column twisting. As beam-skew increased column twist increased, and the resulting plastic strains at the column flange-tip increased.

Plastic strain distributions along the lower beam-flange to column-flange interface (see Figure 28 and Figure 29) were seemingly unaffected by increases in column axial load for each of the column configurations (see Figure 30). Only the plastic strains along the acute angle between the beam and column are presented, as these strains are more severe for every simulation (see again the sample plastic strain contours in Figure 28). From Figure 30, increases in connection plastic strains are dominated by increases in beam skew, with little variation due to the increases in axial load. Additional plastic strain distributions at 0.04rad drift for each column configuration are shown in Figure 31. Strain distributions resulting at higher story drifts are included in Appendix A.
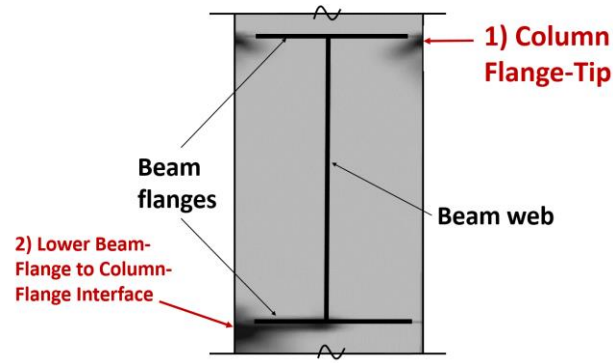
Figure 28 Two common areas of maximum equivalent plastic strains (shaded).
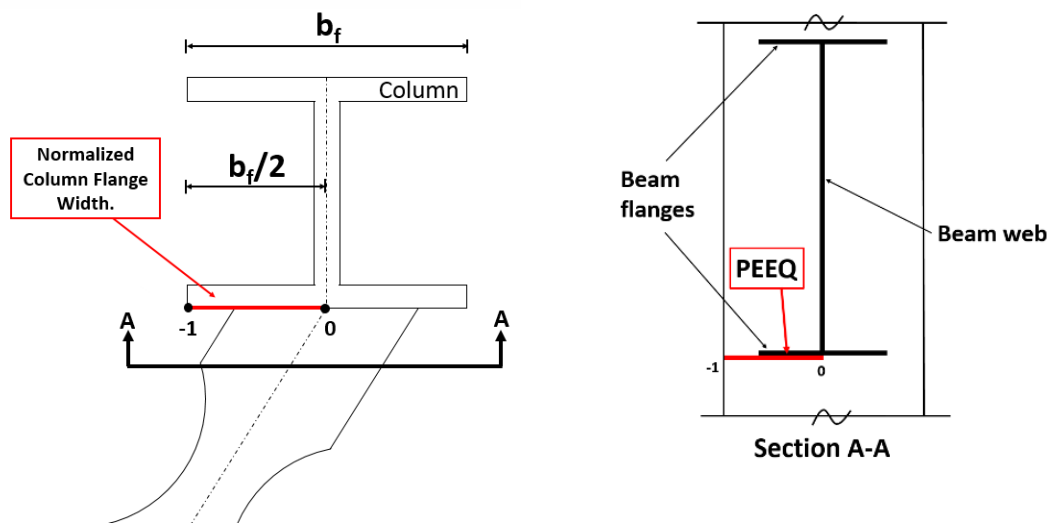
Figure 29 Location of data extraction for column-flange PEEQ distribution.
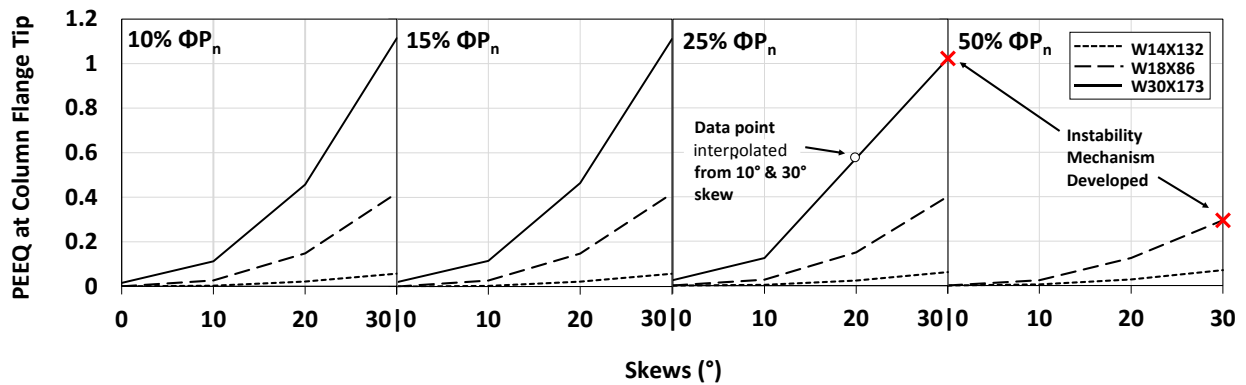
Figure 30 Effect of beam-skew and axial load on the PEEQ at the column flange-tip at 0.04 rad drift.
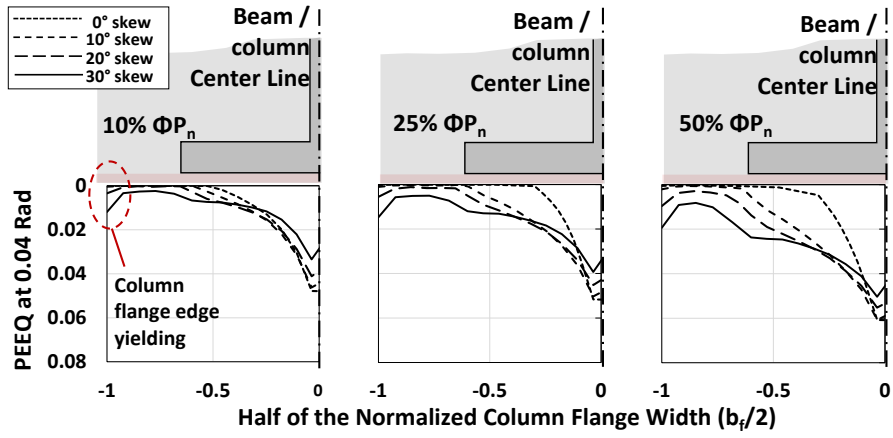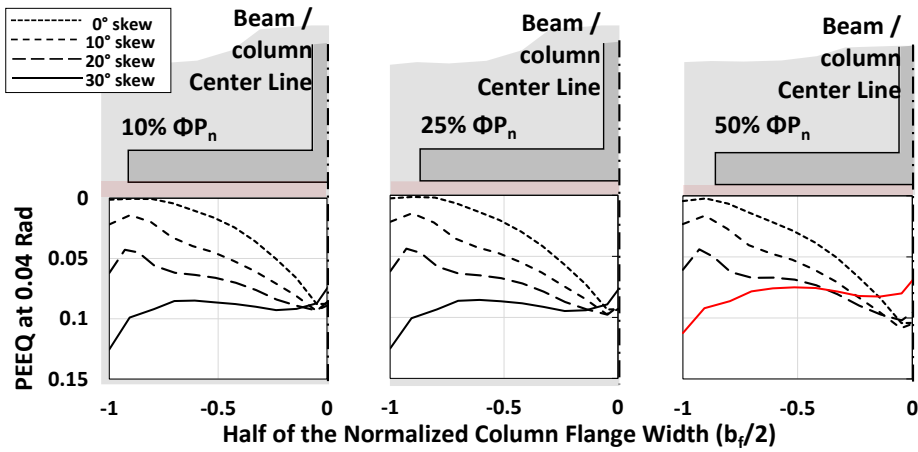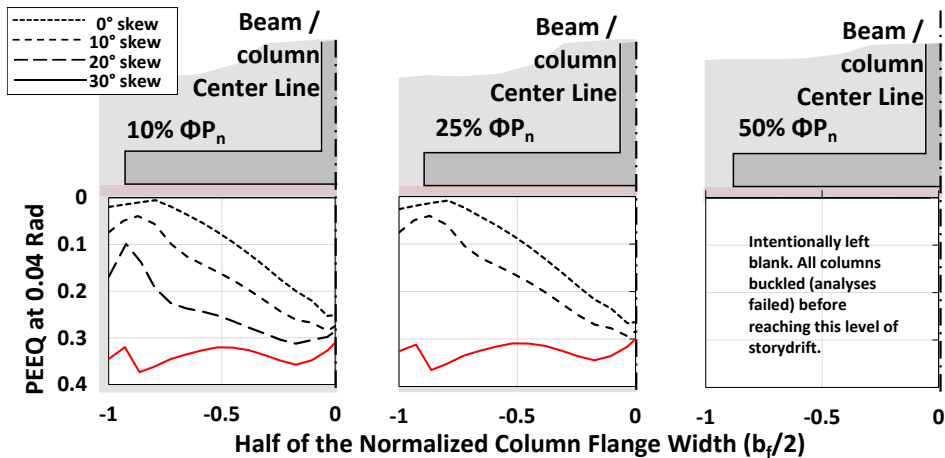
Figure 31 PEEQ distribution along the normalized deep-column flange with varying skews and axial loads at 0.04 rad drift. (a) W 14×132 models; (b) W18×86 models; and (c) W30×173 models. The red lines denote the presence of column local buckling.

4. Summary and Conclusions

The effect of column axial loads on the performance of SMFs containing skewed RBS connections was investigated using detailed finite element analyses. A total of 48 analyses were performed, representing 3 beam-column configurations, 4 levels of beam skew, and 4 levels of column axial load. All considered beam-column geometries narrowly satisfy slenderness limits as outlined in the AISC Seismic Provisions, representing worst-case scenarios for performance evaluation. The following conclusions are based on the 48 analyses:

1. Increasing beam-skew and axial load has little effect on connection moment capacity prior to column local buckling initiation.

2. Increasing column axial load (up to 50% ΦP_n) has a negligible effect on resulting column twist. Beam-skew angle is the dominate contributor to resulting column twist.

3. Applied column axial loads have little effect on column flange yielding within the beam-to-column connections. Column flange yielding is dominated by the applied beam-skew angle.

4. Deep-column SMFs are susceptible to column local buckling at low beam-skew angles. Under the larger applied axial loads (50% ΦP_n) column local buckling was observed in the deep-column configurations at low drifts (less than 0.04rad) and at all beam skew angles. It is important to note that the medium-depth columns also experienced local buckling issues at low drifts (less than 0.04rad); however, this only occurred at large beam-skew angles (greater than 20deg) and large axial loads.

References

ABAQUS, (2015), Abaqus Analysis User's Manual, version 6.12, University at Cambridge, UK.

American Institute of Steel Construction, (2010a). Code of standard practice for steel buildings and bridges, Chicago.

American Institute of Steel Construction, (2010b), ANSI/AISC 341-05. Seismic provisions for structural steel buildings, American Institute of Steel Construction, Inc., Chicago, IL.

American Institute of Steel Construction, (2011), Steel Construction Manual, 14th edition. AISC, Chicago, IL.

American Institute of Steel Construction, (2012), Seismic Design Manual, 2nd edition. Structural Educational Council, Chicago, IL.

Chi, W., Kanvinde, A., and Deierlein, G. (2006). "Prediction of Ductile Fracture in Steel Connections Using SMCS Criterion." *J. Struct. Eng.* 132(2), 171-181.

Chi, B., & Uang, C. M. (2002). Cyclic response and design recommendations of reduced beam section moment connections with deep columns. *Journal of Structural Engineering*, 128(4), 464-473.

Earthquake Country Alliance. (2003). Retrieved January 18, 2017, from http://www.earthquakecountry.org/step4/steelframe.html

Engelhart, M. D., & Sabol, T. A. (1997, September). Seismic-resistant steel moment connections: Developments since the 1994 Northridge earthquake. Progress in Structural Engineering and Materials, 68-77. doi:10.1002/pse.2260010112

FEMA (2000). Recommended seismic design criteria for new steel moment frame buildings, FEMA 350, Federal Emergency Management Agency, Washington, DC.

Gilton, C. S., and Uang, C.-M. (2002). "Cyclic Response and Design Recommendations of Weak-Axis Reduced Beam Section Moment Connections." *J. Struct. Eng.* 128(4), 452.

Hamburger, Ronald O., Krawinkler, Helmut, Malley, James O., and Adan, Scott M. (2009). "Seismic design of steel special moment frames: a guide for practicing engineers," NEHRP Seismic Design Technical Brief No. 2, National Institute of Standards and Technology, Gaithersburg, MD., NIST GCR 09-917-3

HKS (Hibbitt, Karlsson, and Sorensen). (2006). *ABAQUS standard users manual, version 6.4*, Providence, RI.

Kaufmann, E. J., Metrovich, B. R., and Pense, A. W. (2001). "Characterization of cyclic inelastic strain behavior on properties of A572 Gr. 50 and A913 Gr. 50 rolled sections." *ATLSS Rep. No. 01-13*, National Center for Engineering Research on Advanced Technology for Large Structural Systems, Lehigh Univ., Bethlehem, PA.

Lee, C., Jeon, S., Kim, J., and Uang, C. (2005). "Effects of Panel Zone Strength and Beam Web Connection Method on Seismic Performance of Reduced Beam Section Steel Moment Connections." *J. Struct. Eng.,* 10.1061/(ASCE)0733-9445(2005)131:12(1854), 1854-1865.

Pachoumis, D. T., Galoussis, E. G., Kalfas, C. N., and Christitsas, A. D. (2009). "Reduced beam section moment connections subjected to cyclic loading: Experimental analysis and FEM simulation." *Eng. Structures* 31(1), 216-223.

Prinz, G. S., and Richards, P.W. (2016) "Demands on reduced beam section connections with out-of-plane skew." *J. Struct. Eng.* 142(1)

Richards, P. W., and Prinz, G. S. (2007). "Non-linear time history analysis of refined mesh steel structures." *Proc., 9th Canadian Conf. on Earthquake Engineering, Canadian Association for Earthquake Engineering*, ON, Canada.

Richards, P. W., and Uang, C.-M. (2005). "Effect of flange width-thickness ratio on eccentrically braced frames link cyclic rotation capacity." *J. Struct. Eng*., 10.1061/(ASCE)0733-9445(2005)131:10(1546), 1546–1552.

Ricles, J. M., Mao, C., Lu, L., & Fisher, J. W. (2003). "Ductile details for welded unreinforced moment connections subject to inelastic cyclic loading". *Engineering Structures*, 667-680. doi:10.1016/s0141-0296(02)00176-1

Tsai, K. C., Wu, S., & Popov, E. P. (1995). "Experimental performance of seismic steel beam-column moment joints." *Journal of Structural Engineering*, 121(6), 925-931.

Uang, C., Ozkula, G., & Harris, J. (2017). "Observations from Cyclic Tests on Deep, Slender Wide-Flange Structural Steel Beam-Column Members." *Engineering Journal*, 54, 45-60. Retrieved March 17, 2017.

Zhang, X., and Ricles, J. M. (2006). "Seismic Behavior of Reduced Beam Section Moment Connections to Deep Columns."" *J. Struct. Eng*., 10.1061/(ASCE)0733-9445(2006)132:3(358), 358–367.

Appendix

A. Distribution of PEEQ along column flange:

Figures 32A, 33A, and 34A display the equivalent plastic strains (PEEQ) along the column

flange for the shallow (W14X132), medium (W18X86), and deep (W30X173) column sections,

respectively. The strains, taken at the elevation just below the bottom flange of the beam on

the acute angle side of the skew (see Figure 29), showed the distribution of yielding as skew

and/or axial load increased. The red lines represent the rotations at which the columns

contained an instability mechanism, usually some degree of column local buckling.
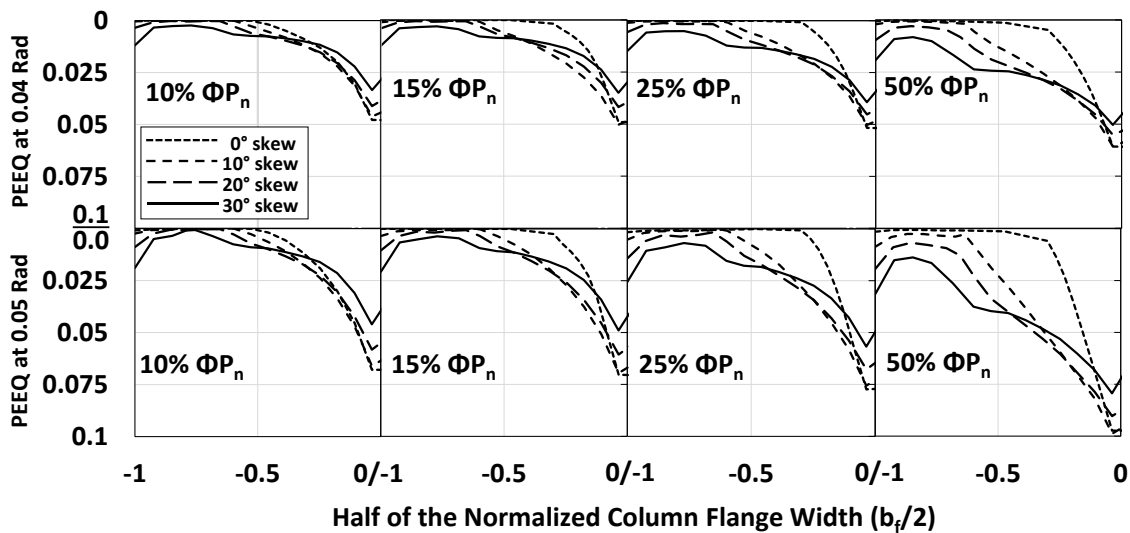
Figure 32A Distribution of PEEQ at 0.04 and 0.05 rad drift with varying skews and axial loads for the shallow-column SMFs.
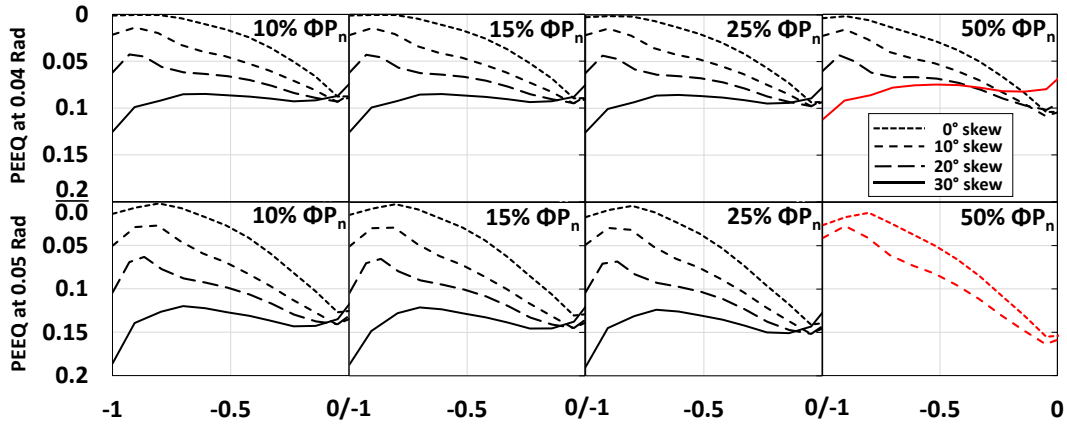
Figure 33A Distribution of PEEQ at 0.04 and 0.05 rad drift with varying skews and axial loads for the medium-column SMFs.
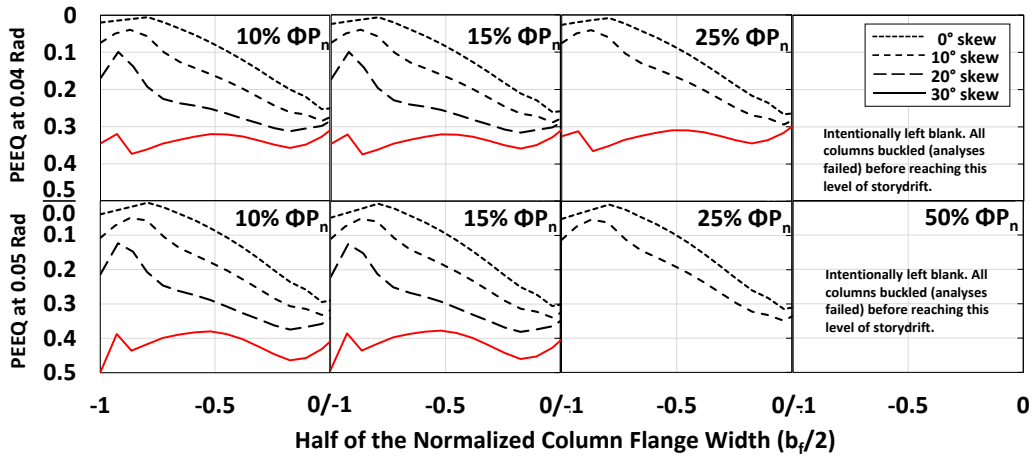
Figure 34A Distribution of PEEQ at 0.04 and 0.05 rad drift with varying skews and axial loads for the deep-column SMFs.

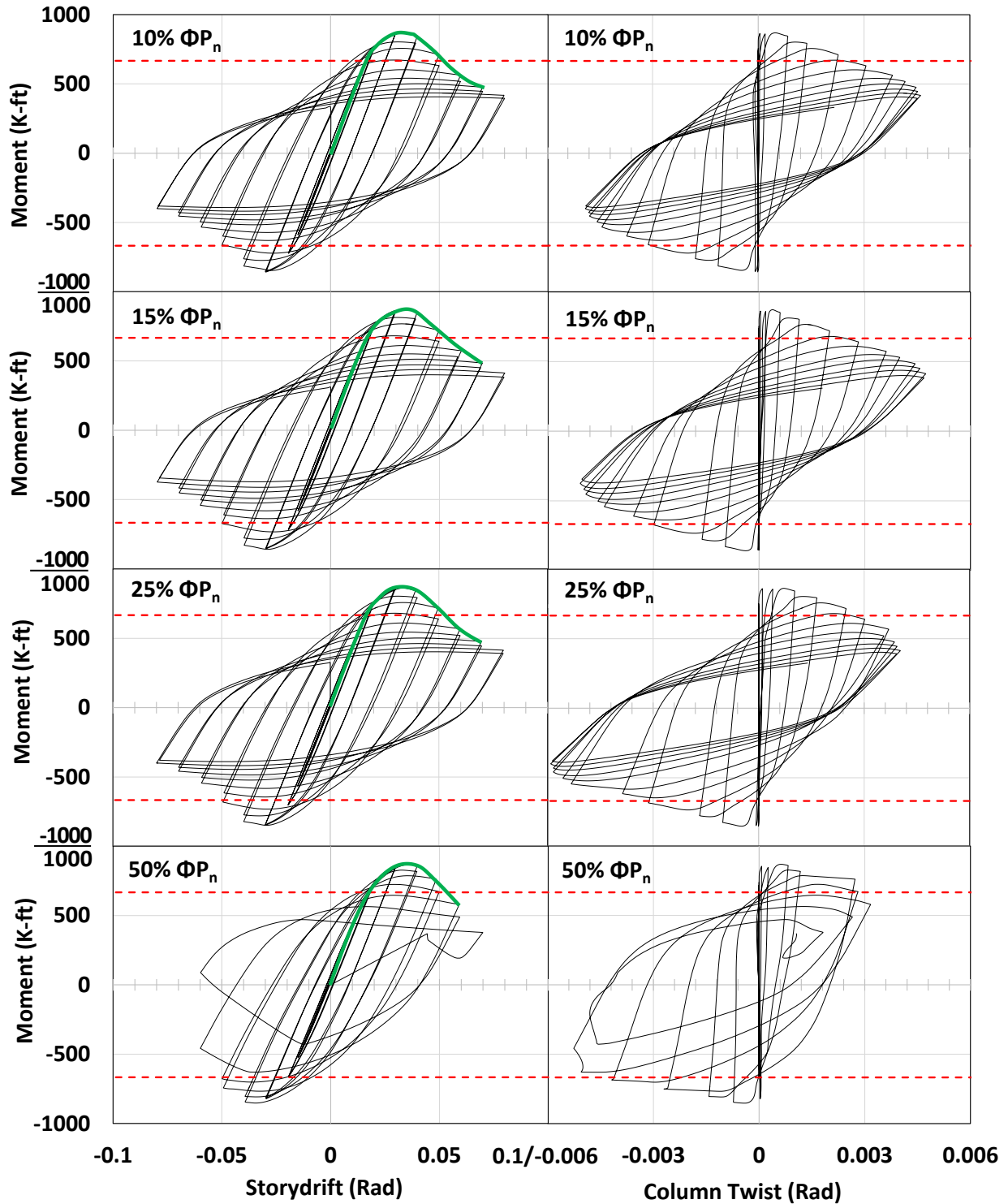## B. Hysteresis graphs:

Figures 35B – 38B, Figures 39B – 42B, and Figures 43B – 46B show the hysteresis graphs for the W14×132 (shallow-column) models, W18×86 (medium-column) models, and W30×173 (deep-column) SMFs at the four different beam skews, respectively. The hysteresis graphs on the left show the connection moments (in K-ft), and the respective storydrifts. The hysteresis graphs on the right show the same connection moments along with the corresponding effect on column twisting. The red dashed-lines are the beam moments (K-ft) representing $0.8M_p$, and the green lines show the approximated backbone curves. The intersection of the red and green lines are the storydrifts obtained at $0.8M_p$, summarized in Table 2.

Figure 35B Hysteresis graphs showing moments and column twist with storydrift for the shallow-column SMFs containing 0° skew.
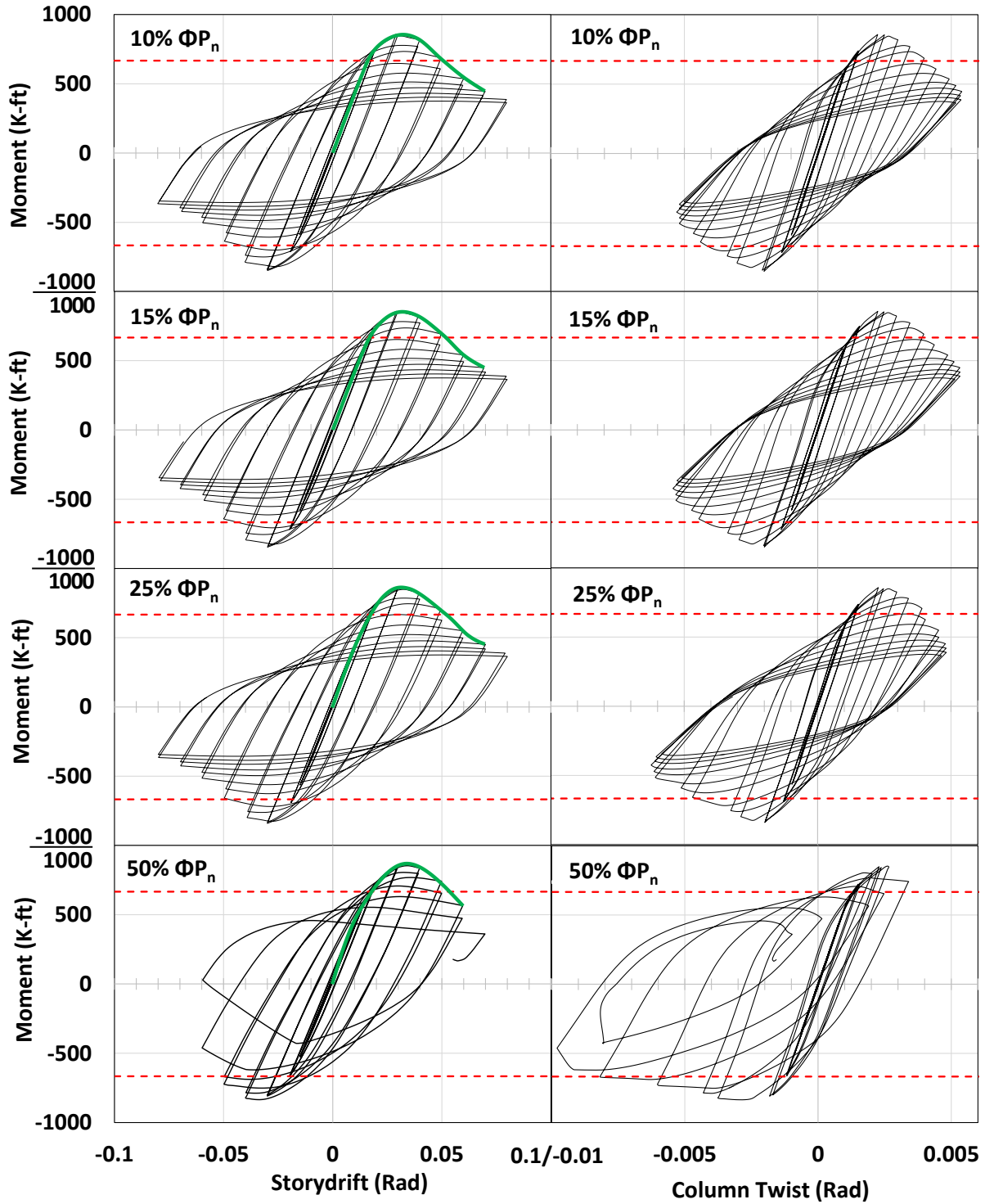
Figure 36B Hysteresis graphs showing moments and column twist with storydrift for the shallow-column SMFs containing 10° skew.

Figure 37B Hysteresis graphs showing moments and column twist with storydrift for the shallow-column SMFs containing 20° skew.
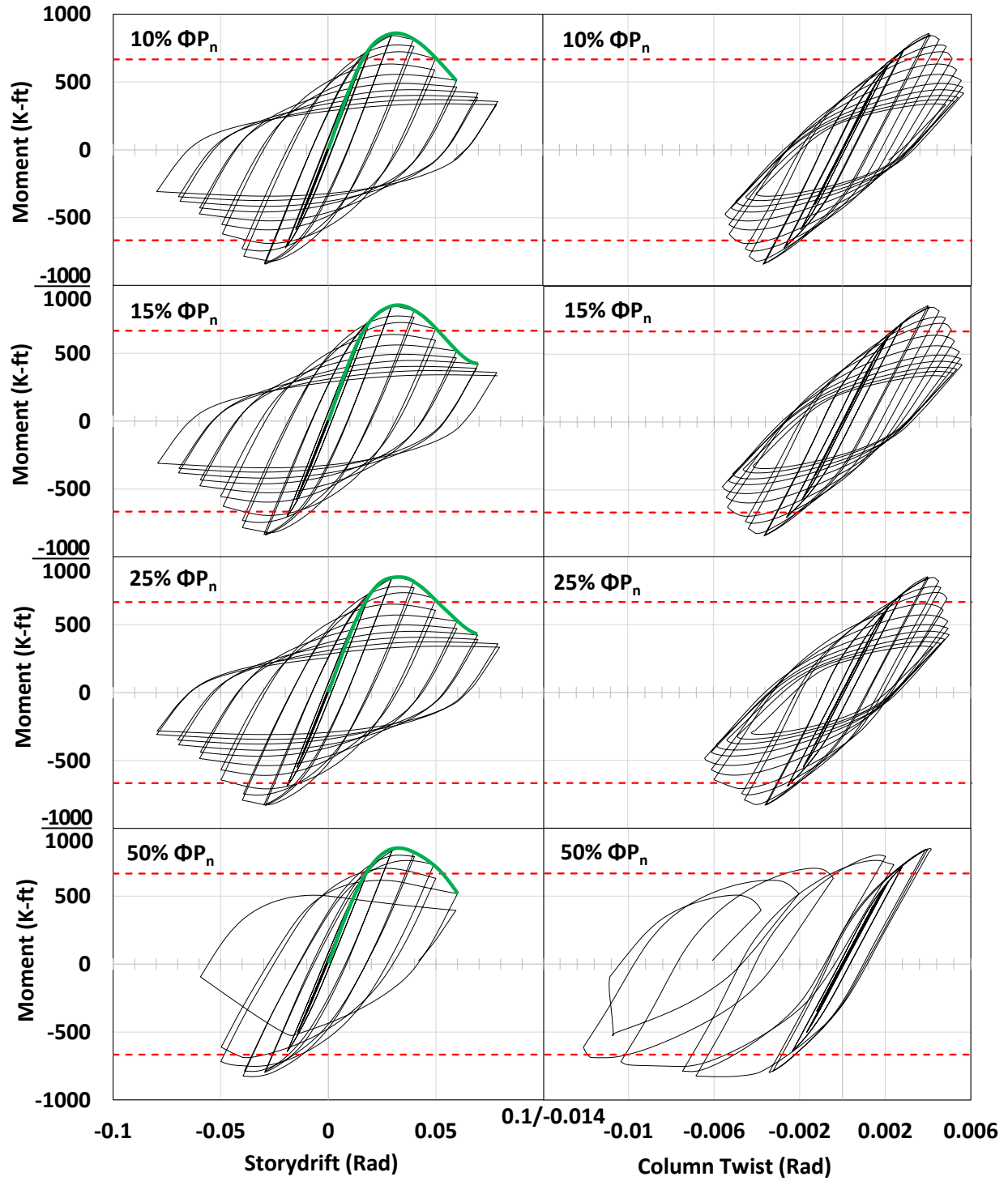
43

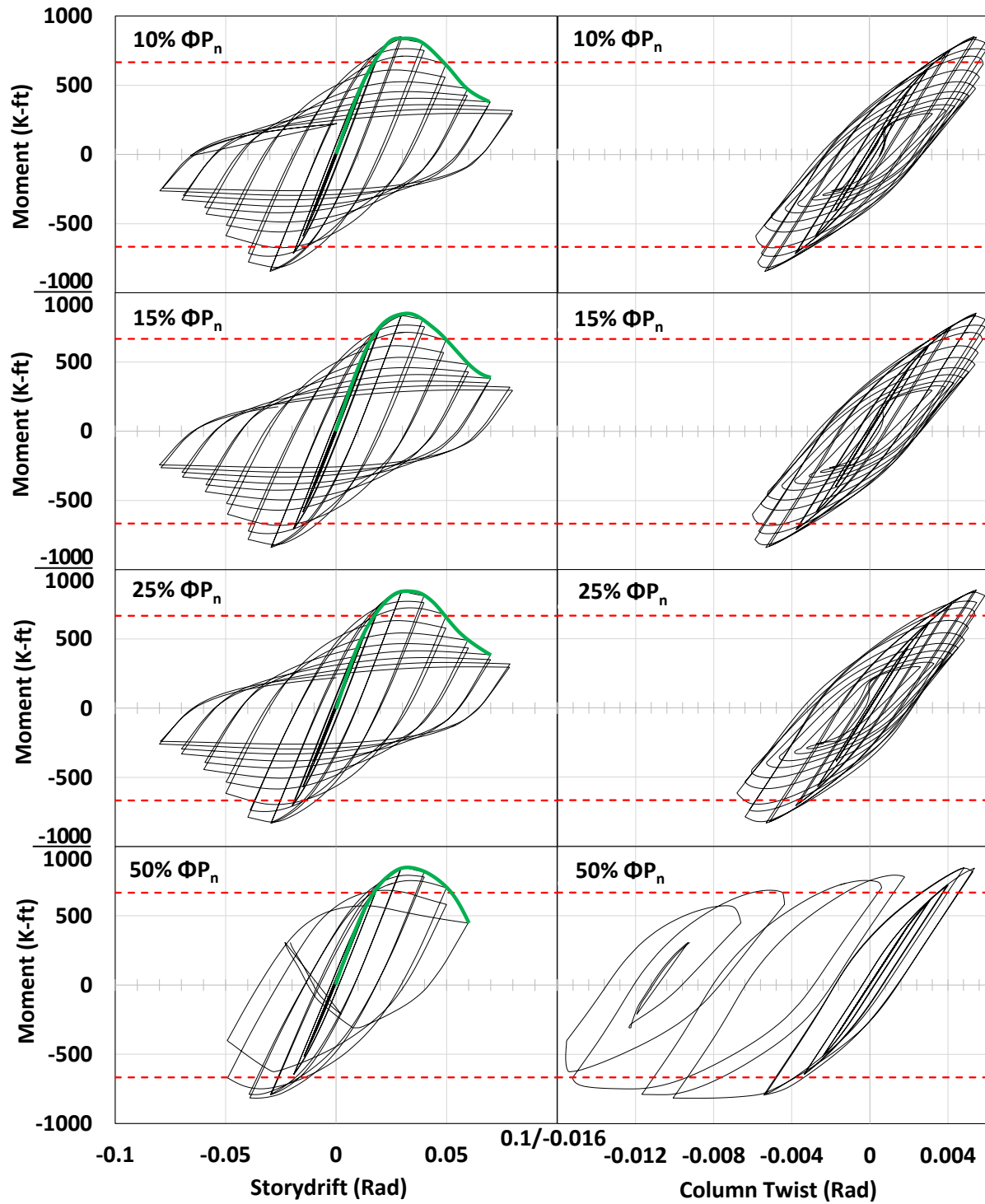***Figure 38B*** Hysteresis graphs showing moments and column twist with storydrift for the shallow-column SMFs containing 30° skew.

Figure 39B Hysteresis graphs showing moments and column twist with storydrift for the medium-column SMFs containing 0° skew.

Figure 40B Hysteresis graphs showing moments and column twist with storydrift for the medium-column SMFs containing 10° skew.

Figure 41B Hysteresis graphs showing moments and column twist with storydrift for the medium-column SMFs containing 20° skew.

47

Figure 42B Hysteresis graphs showing moments and column twist with storydrift for the medium-column SMFs containing 30° skew.
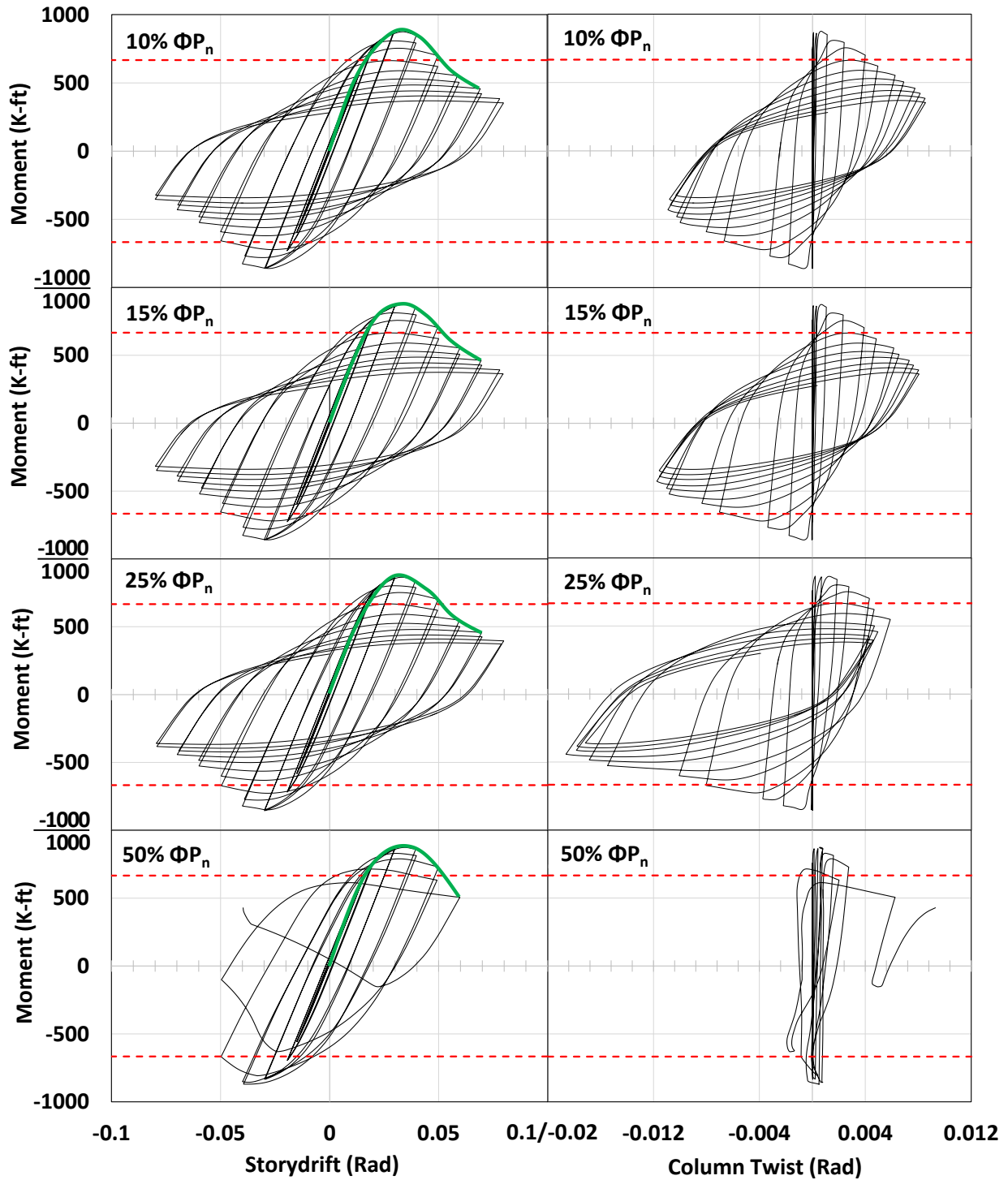
48

Figure 43B Hysteresis graphs showing moments and column twist with storydrift for the deep-column SMFs containing 0° skew.

49

Figure 44B Hysteresis graphs showing moments and column twist with storydrift for the deep-column SMFs containing 10° skew.
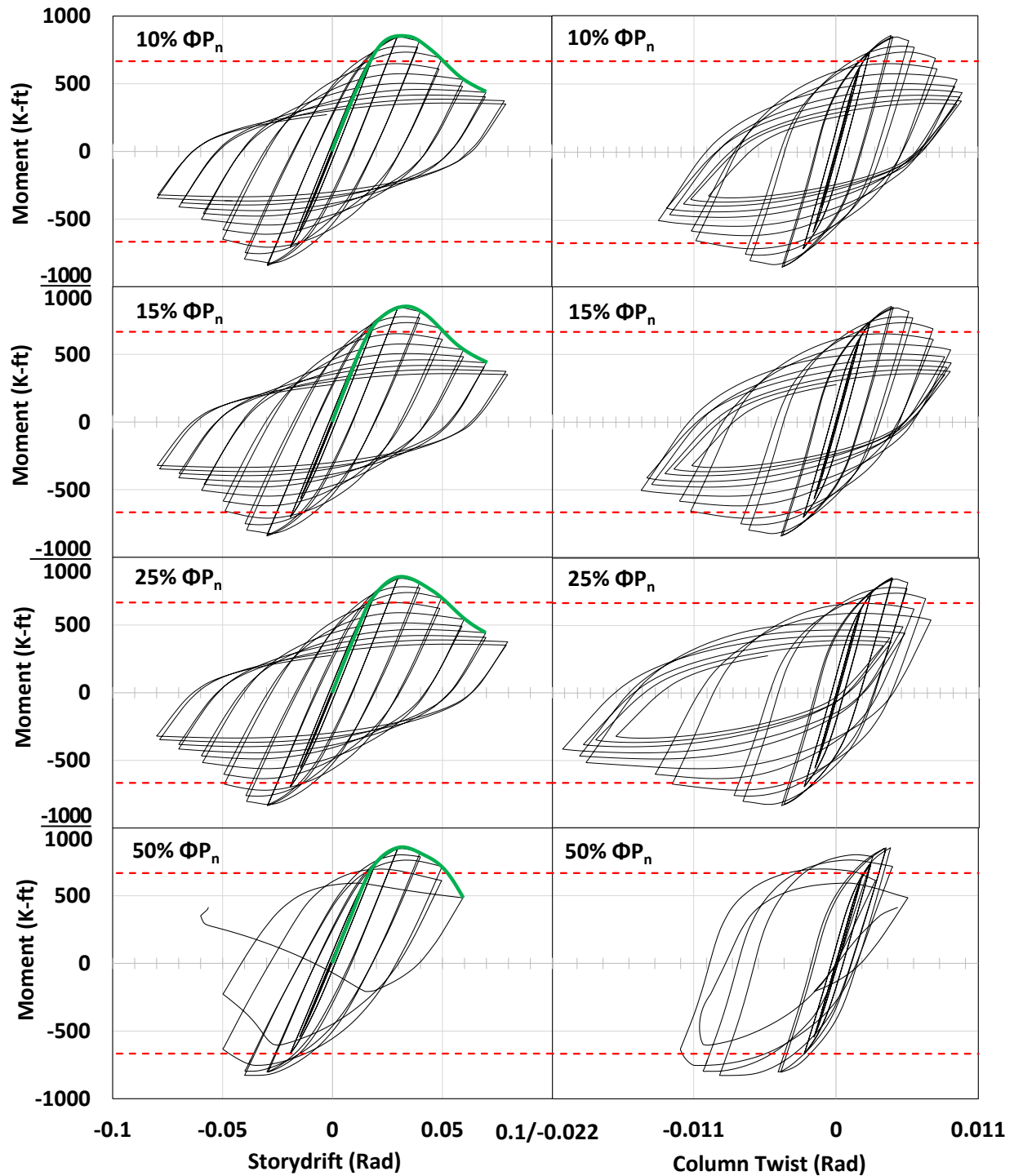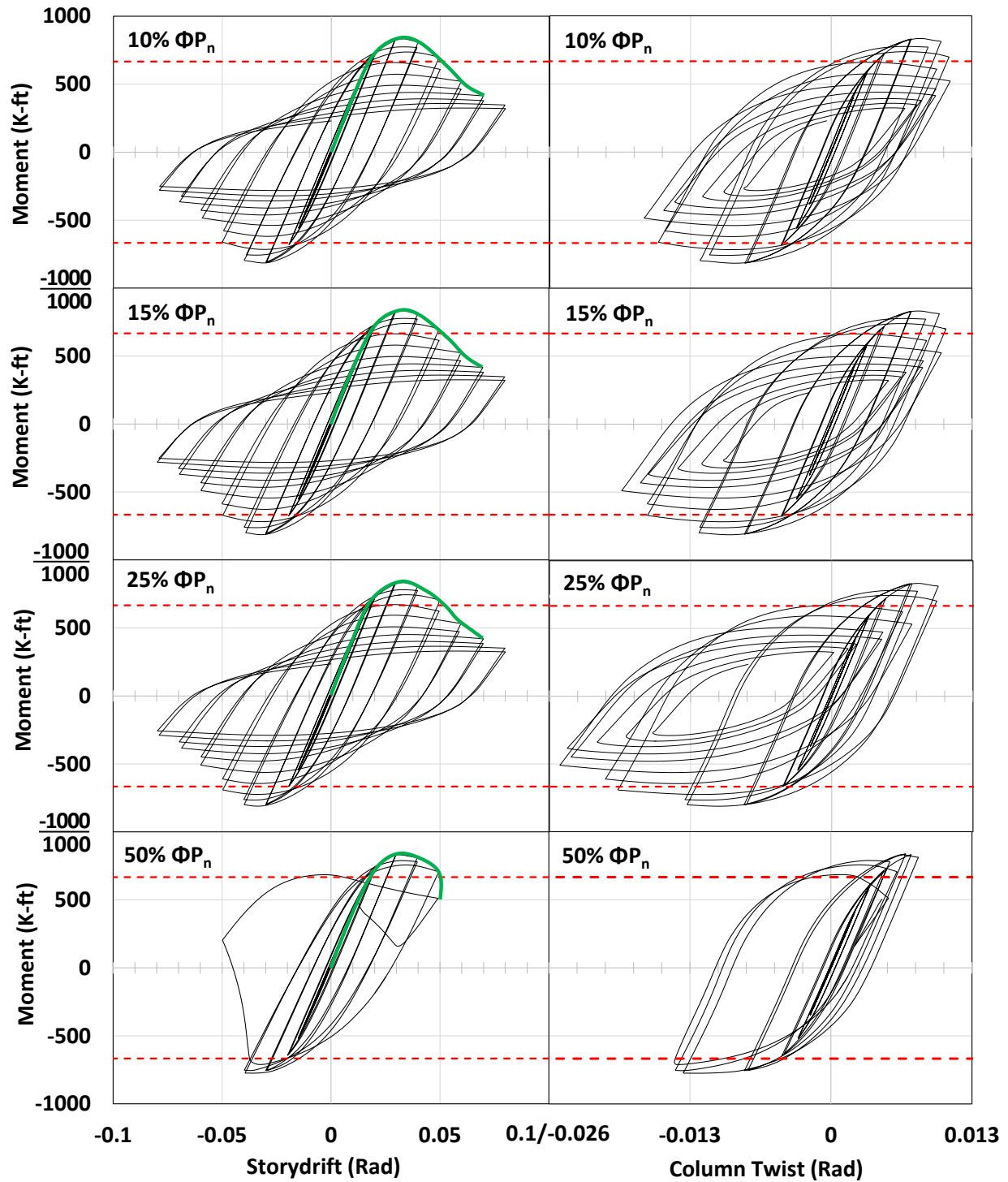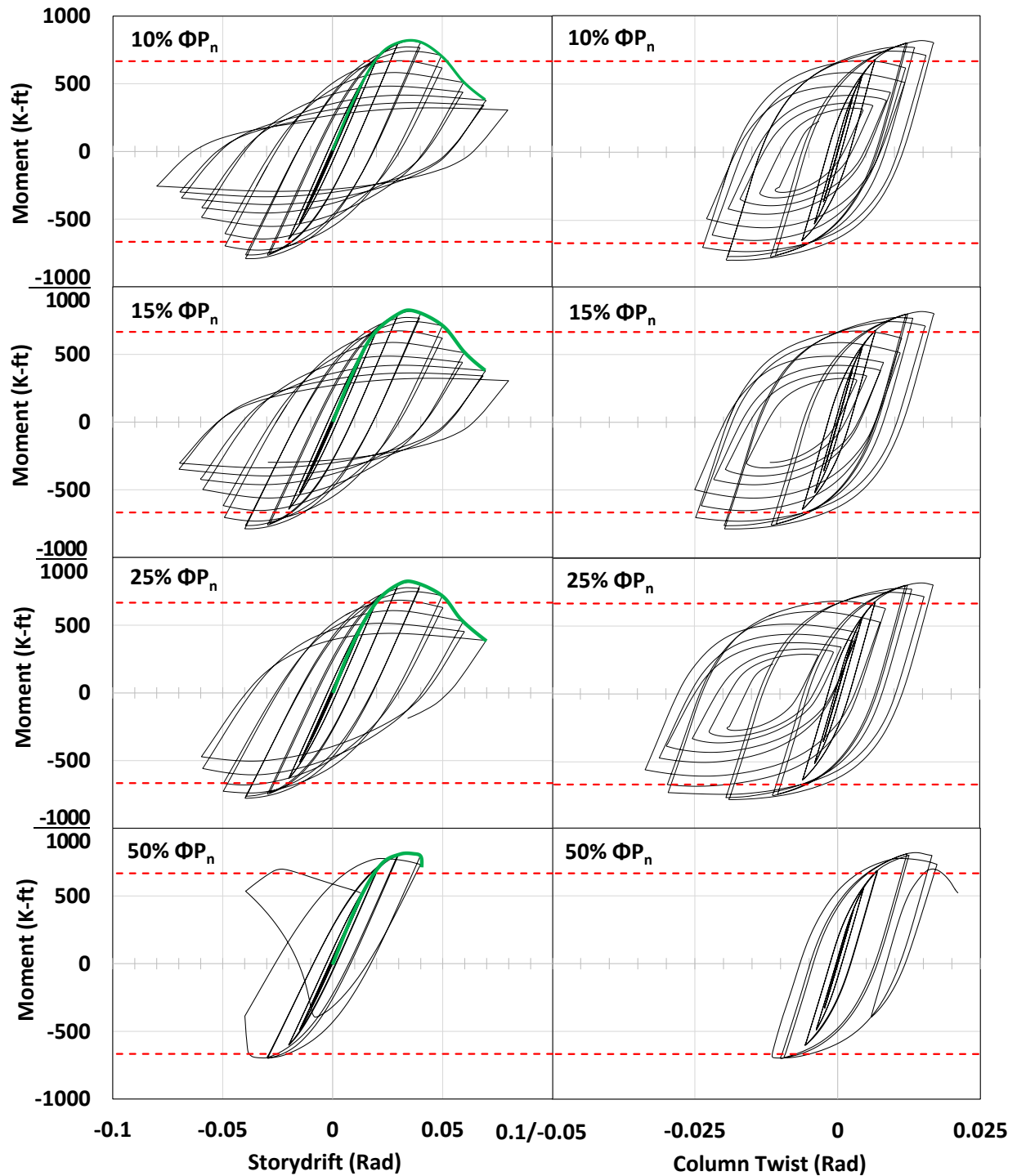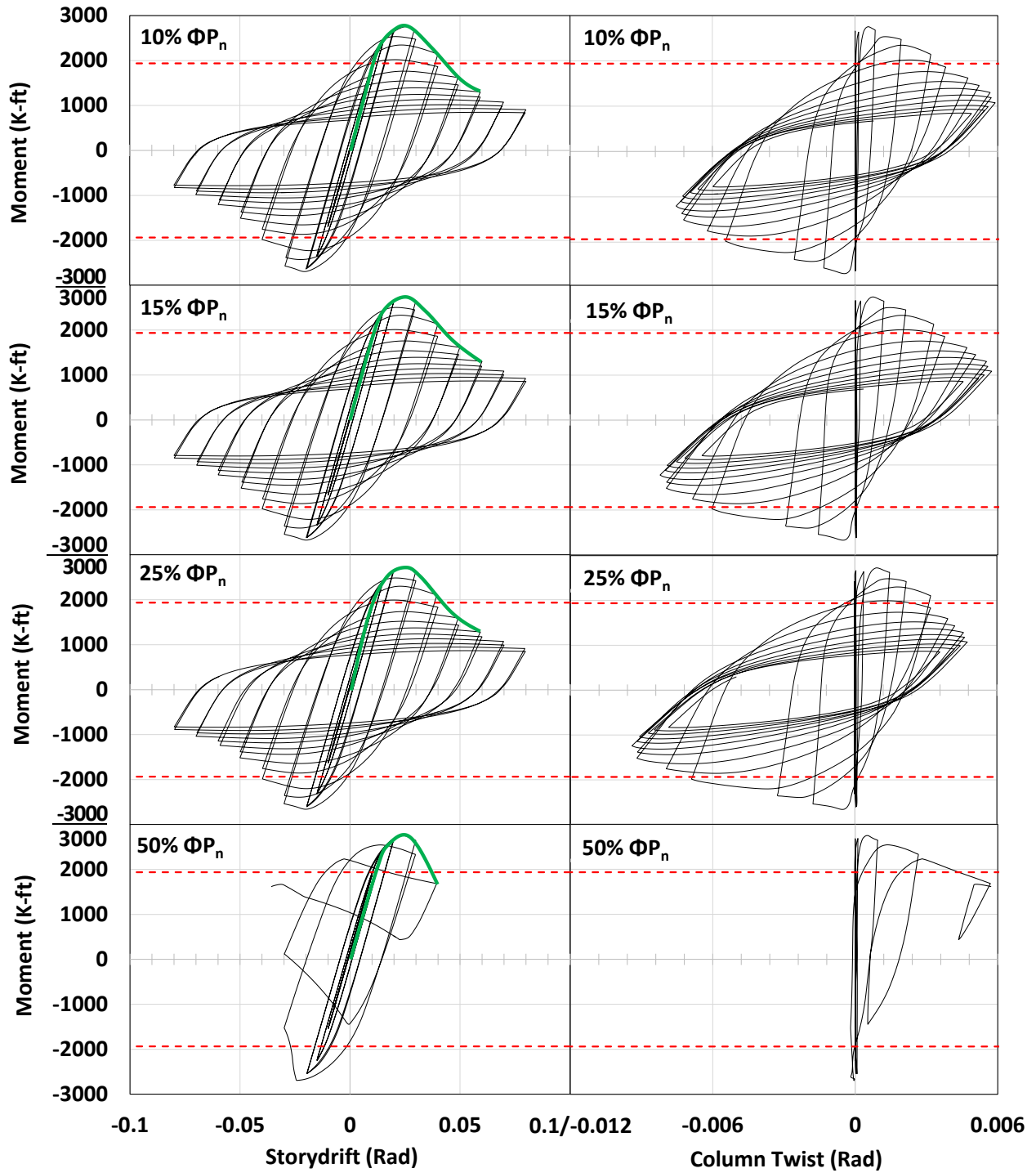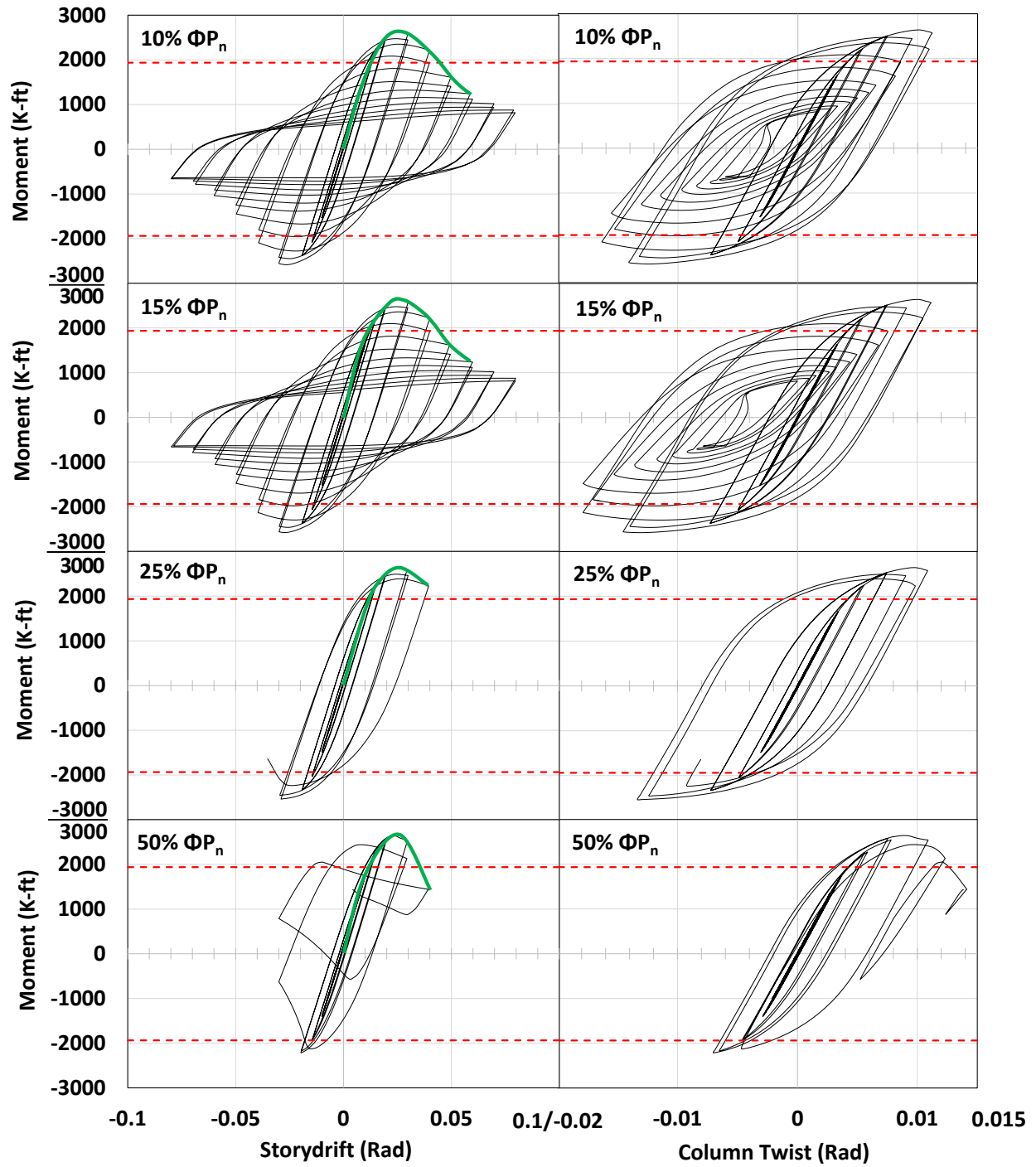
Figure 45B Hysteresis graphs showing moments and column twist with storydrift for the deep-column SMFs containing 20° skew.
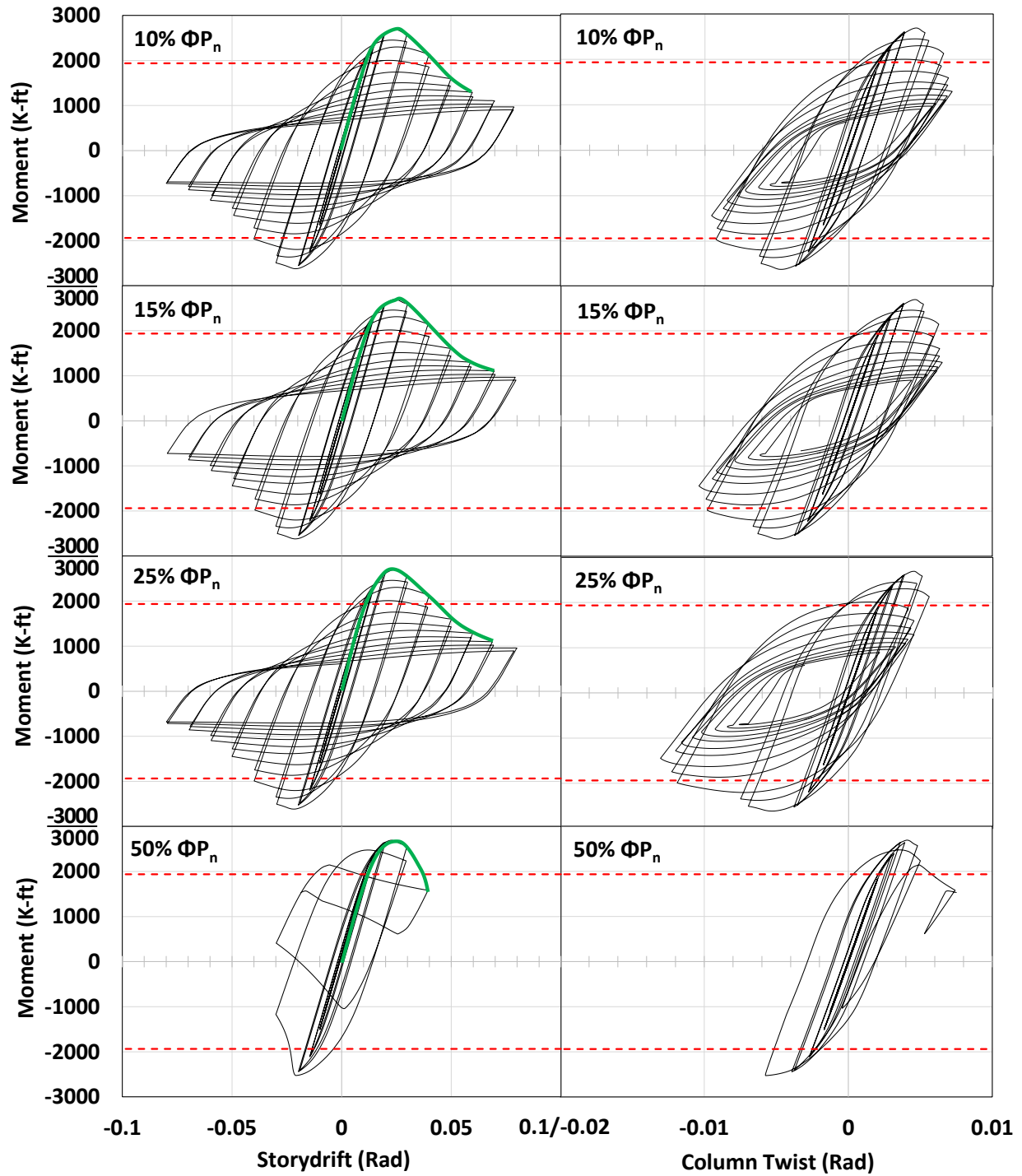
51
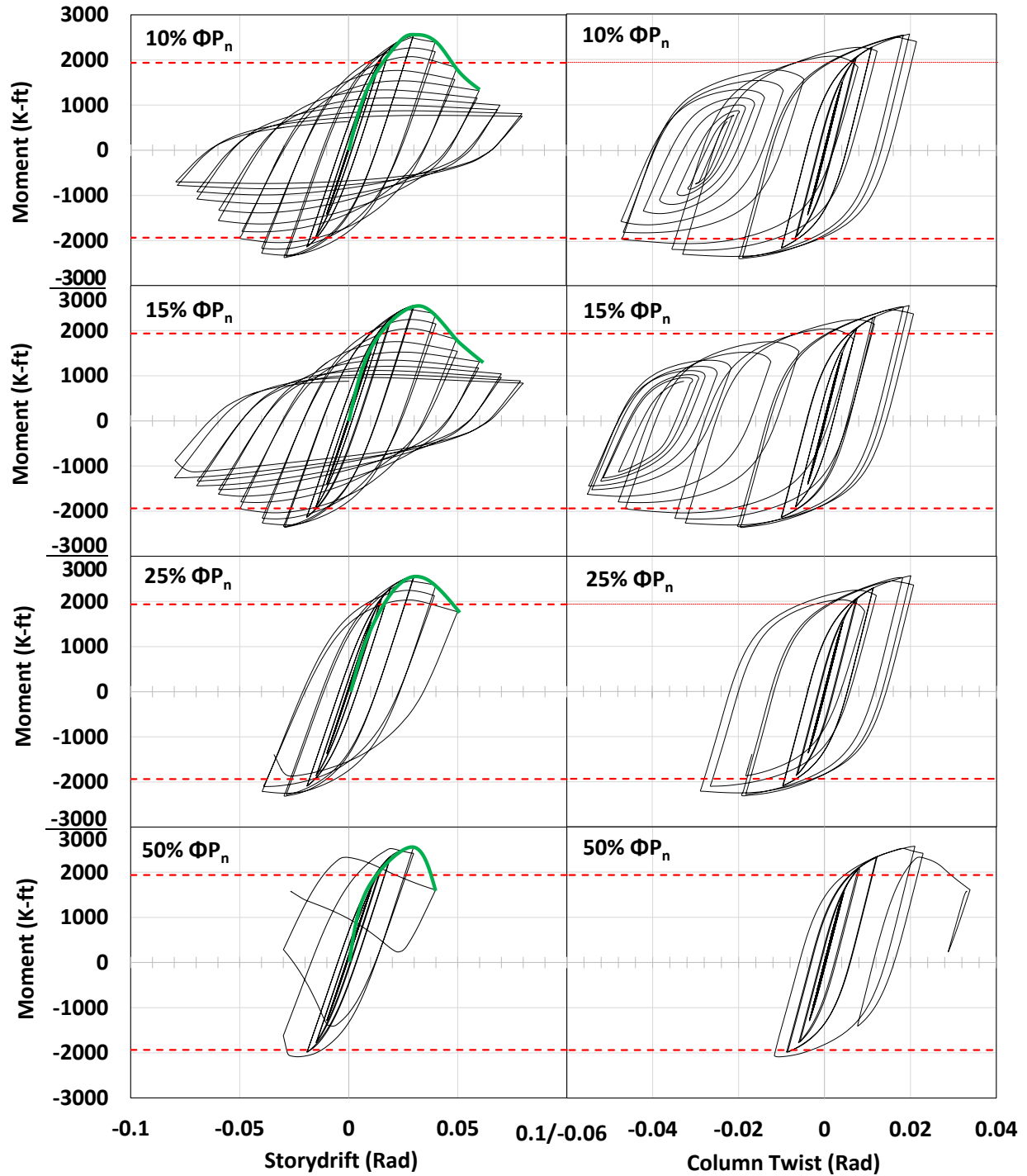
Figure 46B Hysteresis graphs showing moments and column twist with storydrift for the deep-column SMFs containing 30° skew.

C. RBS flange-cut dimension calculations:

The following section outlines the iterative process of calculating the RBS flange-cut

dimensions as outlined in AISC seismic design manual (2012). The process is summarized in

three steps once the beam and columns have been selected:

1. Assume the values for "a", "b", and "c" based on dimension limits provided in the AISC Seismic Provisions (AISC, 2012).

2. Calculate the moment at the column flange (M_f) resulting from the plastic moment in the RBS (M_{PR}), as shown in Figure 46C.

3. Make sure the induced moment (M_f) is less than the moment capacity (M_{Pf}) at the column face.
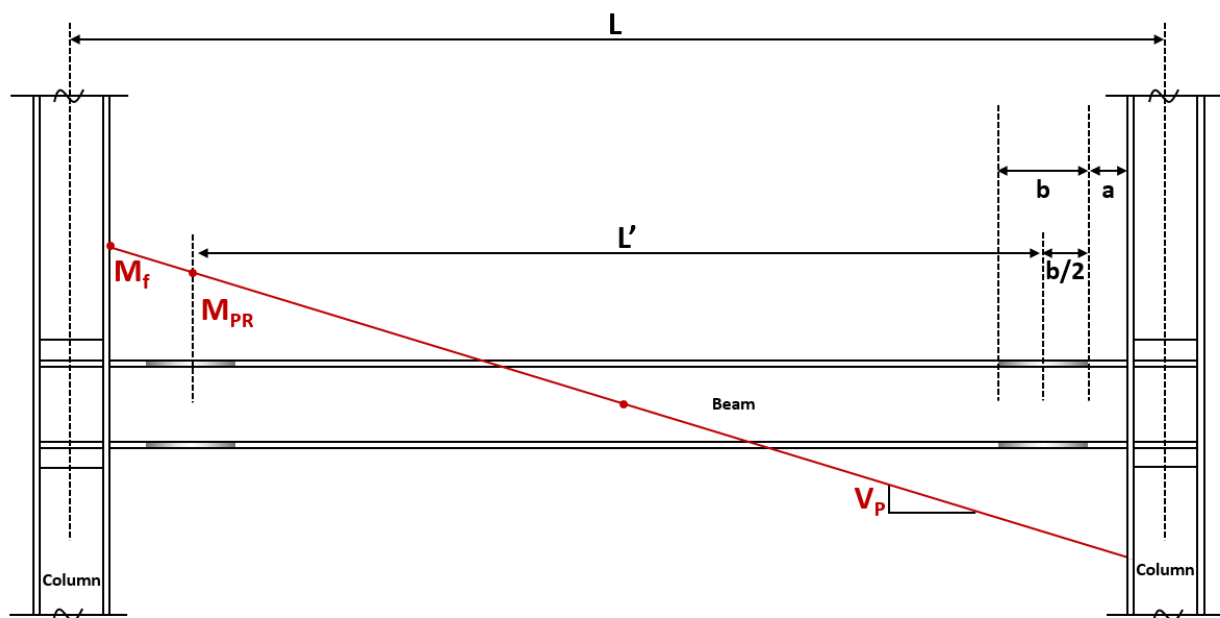
Figure 47C Visualization of moment distribution along the beam and the influence of the plastic moment in the RBS moment (M_{PR}) on the moment at the column face (M_f).

1. Assuming a, b, and c:

    Beam (W24×76) properties: b_f = 8.99 in, d_b = 23.9 in, t_f = 0.68 in, Z_x = 200 in^3

    Column (W14×132) properties: d_c = 14.7 in

    Limits: $0.5b_f \le a \le 0.75b_f$ → $4.0 \le a \le 6.74$

                             $0.65d_b \le b \le 0.85d_b$ → $15.54 \le b \le 20.31$

                             $0.1b_f \le c \le 0.25b_f$ → $0.9 \le c \le 2.24$

    Initial assumptions: **a** = 6 in, **b** = 18 in, and **c** = 1.5 in

2. Calculate the moments at the column flange (M$_f$) induced by the RBS plastic moment (M$_{PR}$).

$$L' = L - 2a - d_c - b \qquad \text{Eq. 2}$$
$$Z_{RBS} = Z_X - (2)(c)(t_f)(d_b - t_f) \qquad \text{Eq. 3}$$
$$M_{PR} = C_{PR}R_Y Z_{RBS}F_Y \qquad \text{Eq. 4}$$
$$V_P = \frac{M_{PR}}{\left(\frac{L'}{2}\right)} \qquad \text{Eq. 5}$$
$$M_f = M_{PR} + (V_P)(a + \frac{b}{2}) \qquad \text{Eq. 6}$$

where "F_Y" is the yield strength of A992 Grade 50 steel, which is 50 Ksi. "L'" is the distance

between the two plastic hinges (middle of the flange cuts), and was found to be 315.3

inches. "Z_X" and "Z_{RBS}" are the plastic section moduli about the axis of bending (X- axis) for

the entire (uncut) section and the reduced section, which were found to be 200 in^3 and

152.63 in^3, respectively. "M_{PR}" is the plastic moment of the RBS, calculated as 10,073.6 K-

in. "C_{PR}" is the strain hardening factor and "R_Y" is the over strength factor of 1.2 and 1.1,

respectively. "V_P" is the shear at the plastic hinge, and was determined to be 63.9 K.

Finally, "M_f" is the moment force at the column face determined from the linear

relationship of the shear force along the beam, and was calculated as 11,032 K-in.

3. Compare to the moment capacity at the column flange (M_{Pf}):

$$M_{Pf} = R_Y Z_X F_Y \qquad \qquad \textbf{Eq. 7}$$

"M_{Pf}" was found to be 11,000 K-in. The limit **M_f < M_{Pf} was not** satisfied, and therefore must start over. To reduce M_f, we can either increase "c" and/or "b", or decrease "a".

1. The new RBS flange cut dimensions will be:

   a = 5.5 in, **b** = 18 in, and **c** = 2 in

2. L' = 316.3 in, Z_{RBS} = 136.84 in³, M_{PR} = 9,031.55 K-in, V_P = 57.11 K, **M_f = 9,859.61 K-in**

3. The limit **M_f < M_{Pf} was** satisfied, therefore:

> **a = 5.5 in, b = 18 in, and c = 2 in**

D. Determination of column nominal compressive strength:

Table 1-2 in the AISC's seismic design manual (2012) shows that all columns and beams used in the models are "seismically-compact" for SMFs. However, the columns must also be checked for additional slenderness ratios since they are also experiencing axial compression. The local buckling slenderness ratios, found in Table B4.1a in AISC steel construction manual (2011), dictate how to determine the "KL/r" ratio which in turn governs which equations used to find the nominal compressive strengths (ΦP_n). The shallow and medium columns passed all of the local buckling ratios from the mentioned table (Q=1). The deep column, however, did not satisfy the slenderness ratio for stiffened elements (i.e. the web) for a yield strength of 50 Ksi. The calculation for its nominal compressive strength, ΦP_n, in this thesis was based on a Q of 1; however, the actual Q is 0.95 considering the stiffened slender web section. This results in a slight discrepancy for the deep column axial loads provided (ie. a 25% ΦP_n as described, considering Q=1, will represent approximately 25.8% ΦP_n when considering a Q of 0.95). Since the slenderness ratio (Eq. 8) was satisfied in all column sections, ΦP_n was found using equations 9-11, gathered from Chapter E in the AISC steel construction manual (2011) for compression members with slender elements:

$$\frac{KL}{R} \leq 4.71\sqrt{\frac{E}{QF_y}} \qquad\qquad \textbf{Eq. 8}$$

$$F_{cr} = Q\left[0.658^{\frac{QF_y}{F_e}}\right]F_y \qquad\qquad \textbf{Eq. 9}$$

$$F_e = \frac{\pi^2 E}{(\frac{KL}{r_y})^2} \qquad\qquad \textbf{Eq. 10}$$

$$\Phi\text{Pn} = (0.9)F_{cr}A_g \qquad\qquad \textbf{Eq. 11}$$

The nominal compressive strengths were found to be 1510, 880, and 1968 Kips for the

shallow (W14×132), medium (W18×86), and deep columns (W30×173), respectively.